

Low- $\delta^{18}\text{O}$ Rhyolites from Yellowstone: Magmatic Evolution Based on Analyses of Zircons and Individual Phenocrysts

ILYA N. BINDEMAN* AND JOHN W. VALLEY

DEPARTMENT OF GEOLOGY AND GEOPHYSICS, UNIVERSITY OF WISCONSIN, 1215 W. DAYTON STREET, MADISON, WI 53706, USA

RECEIVED MAY 24, 2000; REVISED TYPESCRIPT ACCEPTED FEBRUARY 8, 2001

The Yellowstone Plateau volcanic field is one of the largest centers of rhyolitic magmatism on Earth. Major caldera-forming eruptions are followed by unusual low- $\delta^{18}\text{O}$ rhyolites. New oxygen isotope, petrologic and geochemical data from rhyolites belonging to the 2.0 my eruptive history of Yellowstone are presented, with emphasis on the genesis of low- $\delta^{18}\text{O}$ magmas erupted after the Huckleberry Ridge Tuff (2.0 Ma, 2500 km³) and Lava Creek Tuff (0.6 Ma, 1000 km³). Analyses of individual quartz and sanidine phenocrysts, obsidian samples and bulk zircons from low- $\delta^{18}\text{O}$ lavas reveal: (1) oxygen isotope variation of 1–2‰ between individual quartz phenocrysts; (2) correlation of zircon crystal size and $\delta^{18}\text{O}$; (3) extreme (up to 5‰) zoning within single zircons; zircon cores have higher $\delta^{18}\text{O}$; (4) $\Delta^{18}\text{O}$ disequilibria between quartz, zircon and homogeneous unaltered host glass where zircon cores and some quartz phenocrysts have higher $\delta^{18}\text{O}$ values. These features are present only in low- $\delta^{18}\text{O}$ intra-caldera lavas that erupted shortly after caldera-forming eruptions. We propose that older, hydrothermally altered, ^{18}O -depleted ($\delta^{18}\text{O} \sim 0\%$), but otherwise chemically similar, rhyolites in the down-dropped block were brought nearer the hot interior of the magma chamber. These rhyolites were remelted, promoting formation of almost totally molten pockets of low- $\delta^{18}\text{O}$ melt that erupted in different parts of the caldera as separate low- $\delta^{18}\text{O}$ lava flows. Alteration-resistant quartz and zircon in the roof rock survived early hydrothermal alteration and later melting to become normal $\delta^{18}\text{O}$ xenocrysts (retaining their pre-caldera $\delta^{18}\text{O}$ values) in the low- $\delta^{18}\text{O}$ magma that formed by melting of hydrothermally ^{18}O -depleted volcanic groundmass and feldspars. Zircon and quartz xenocrysts exchanged oxygen with newly formed melt through diffusion and overgrowth mechanisms leading to partial or complete isotopic re-equilibration. Modeling of the diffusive exchange of zircon and quartz during residence in low- $\delta^{18}\text{O}$ magma explains $\delta^{18}\text{O}$ and $\Delta(\text{Qz}-\text{Zrc})$ disequilibria. The

exchange time to form zoned zircons is between a few hundred and a few thousand years, which reflects the residence time of low- $\delta^{18}\text{O}$ magmas after formation and before eruption.

KEY WORDS: Yellowstone; caldera; isotope disequilibria; zircon; $^{18}\text{O}-^{16}\text{O}$

INTRODUCTION

Low- $\delta^{18}\text{O}$ magmas and their abundance

Meteoric water is involved in sub-solidus exchange and in magma genesis of many shallow plutonic bodies and volcanic caldera complexes (Friedman *et al.*, 1974; Muehlenbachs *et al.*, 1974; Hildreth *et al.*, 1984; Criss & Taylor, 1986; Taylor, 1986; Gilliam & Valley, 1997). The more abundant hydrothermally altered rocks are characterized by irregular and large $\Delta^{18}\text{O}$ fractionations between phenocrysts and glass. Low- $\delta^{18}\text{O}$ magmas are recognized by smaller fractionations, consistent with last equilibration at magmatic temperatures, suggesting their original crystallization from ^{18}O -depleted magmas. Low- $\delta^{18}\text{O}$ magmas with $\delta^{18}\text{O}(\text{WR}) < 5.5\%$ (where WR indicates whole rock) are depleted in ^{18}O below the values attainable by normal mantle-derived magmas. Their genesis requires that tens of per cent of total oxygen must

*Corresponding author. Telephone: 608 262 7118. Fax: 608 262 0693. E-mail: inbindem@geology.wisc.edu

ultimately be derived from, or exchanged with, surface waters.

The origin of low- $\delta^{18}\text{O}$ magmas has been proposed to require either direct, sometimes 'catastrophic' addition of meteoric water to magma (Friedman *et al.*, 1974; Hildreth *et al.*, 1984), or more gradual, multistage assimilation of hydrothermally altered rocks (Taylor, 1986; Hildreth *et al.*, 1991), especially by hot, water-undersaturated magmas with large assimilation potential (Balsley & Gregory, 1998). Bacon *et al.* (1989) demonstrated that ^{18}O depletion of normal- $\delta^{18}\text{O}$ magma may proceed through bulk assimilation and be facilitated by partial melting of pre-existing ^{18}O -depleted country rocks surrounding the magma chamber.

Permeable hydrogeological conditions in shallow extensional environments such as rifts, or calderas, coupled with proximity to magma, favor formation of low- $\delta^{18}\text{O}$ magmas (Larson & Taylor, 1986). Calderas are important loci of large-scale fluid-rock isotopic exchange. The best and most extreme example of low- $\delta^{18}\text{O}$ rhyolites occurs in the Yellowstone Plateau volcanic field, Wyoming, where dramatic ($>5\%$) $\delta^{18}\text{O}$ depletions occur in magmas erupted after caldera-forming eruptions. Such extreme depletions are not observed anywhere else in the world. Smaller decreases of 1–2‰ in $\delta^{18}\text{O}$ are more typical for magmas in other caldera complexes and associated plutonic bodies (Friedman *et al.*, 1974; Lipman & Friedman, 1975; Gilliam & Valley, 1997; Balsley & Gregory, 1998; Bindeman *et al.*, 2001b; Monani & Valley, 2001). Although the Yellowstone-scale $\delta^{18}\text{O}$ depletions are yet to be found in other calderas, we believe that the presence of surface-derived water and hence surface-derived oxygen in magmas may be a general feature of calderas world-wide. Small (1–2‰) depletions would be difficult to recognize because many silicic magmas are originally enriched above $\delta^{18}\text{O}(\text{WR}) = 5.5\%$. Identification of such rocks awaits comparative studies of $\delta^{18}\text{O}$ composition in pre-caldera, post-caldera and extra-caldera rocks.

Yellowstone Plateau volcanic field

The Yellowstone Plateau volcanic field is one of the largest centers of silicic magmatism on Earth (Fig. 1). Voluminous ignimbrite eruptions, each followed by caldera collapse, occurred at 2.053 ± 0.006 , 1.304 ± 0.011 and 0.640 ± 0.002 Ma, producing the Huckleberry Ridge Tuff (HRT, $\sim 2500 \text{ km}^3$), Mesa Falls Tuff (MFT, $\sim 300 \text{ km}^3$) and Lava Creek Tuff (LCT, $\sim 1000 \text{ km}^3$), respectively (Christiansen, 1982, 1989; quoted $^{40}\text{Ar}/^{39}\text{Ar}$ ages are from M. A. Lanphere *et al.*, personal communication, 2001). Voluminous and variably ^{18}O -depleted rhyolites, predominantly lava and domes, erupted between tuff eruptions; the volume of intra-caldera lavas following the eruption of LCT alone is at least $\sim 900 \text{ km}^3$

(Christiansen, 1989). Basalts represent $<5\%$ of all volcanic rocks, are mostly extra-caldera, and have normal, mantle-like $\delta^{18}\text{O}(\text{WR})$ of $\sim 6\%$ (Hildreth *et al.*, 1991). Therefore, the Yellowstone system provides a unique opportunity to study the genesis of low- $\delta^{18}\text{O}$ magma.

Although the last eruption at Yellowstone occurred ~ 70 ky ago (Obradovich, 1992), vigorous hydrothermal activity still occurs inside and outside of the 0.6 Ma Yellowstone caldera. Drilling has revealed the existence of modern hydrothermal circulation and steep temperature gradients (70–200°C/km), in all parts of the caldera, with most of the heat flux resulting from hydrothermal flow (Fournier, 1989). Meteoric waters in equilibrium with secondary minerals in drill holes and hot springs are shifted upwards by up to 10‰ in $\delta^{18}\text{O}$ relative to the average present-day value on the surface of -17% (Sturchio *et al.*, 1990). Hydrothermal waters are also enriched in many trace elements leached from rhyolite (Sturchio *et al.*, 1986; Lewis *et al.*, 1997).

Friedman *et al.* (1974) and Hildreth *et al.* (1984) recognized unaltered Yellowstone rhyolites with unusually low $\delta^{18}\text{O}$, and suggested that the low- $\delta^{18}\text{O}$ values resulted from the crystallization of low- $\delta^{18}\text{O}$ magmas in which tens of per cent of total oxygen had exchanged directly or indirectly with meteoric water. The most depleted lavas show dramatic 3 and 5‰ drops in $\delta^{18}\text{O}$, and erupted after the HRT and LCT caldera-forming eruptions (Hildreth *et al.*, 1984). These magmas are referred to as 'low- $\delta^{18}\text{O}$ ', and are the main focus of this study.

Objectives of the present study: a high-resolution look at low- $\delta^{18}\text{O}$ magmas

In this work we report oxygen isotope analyses of over 380 individual phenocrysts and bulk zircon separates from 25 lavas spanning Yellowstone's 2 my eruptive sequence.

Recent advances in the microanalysis of stable isotope ratios (see Rumble & Sharp, 1998; Valley *et al.*, 1998a; and therein) have made it possible to analyze mineral grains individually, including refractory phases such as zircon (e.g. Valley *et al.*, 1994). Earlier conventional techniques required multiple grains of a mineral, thus averaging any intercrystalline or intracrystalline $\delta^{18}\text{O}$ differences. Laser fluorination and ion microprobes provide a new high-resolution look at the classic problem of the genesis of low- $\delta^{18}\text{O}$ rhyolites at Yellowstone, and allow us to reinterpret many aspects of low- $\delta^{18}\text{O}$ magma petrogenesis (Bindeman & Valley, 2000).

Zircon $\delta^{18}\text{O}$ analyses proved to be crucial for reinterpreting the petrogenesis of Yellowstone lavas (Bindeman & Valley, 2000). The ubiquitous presence of zircon as an early crystallizing, near-liquidus mineral in

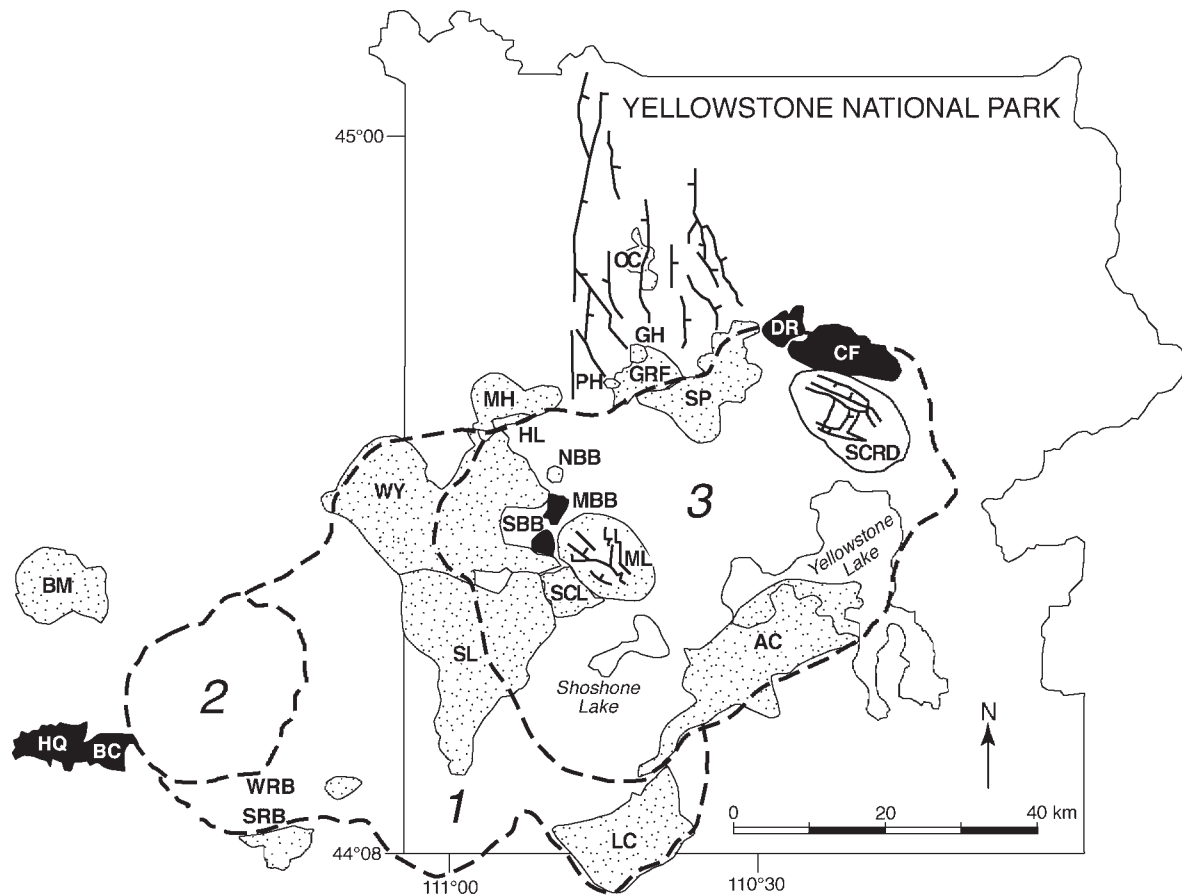


Fig. 1. Map of Yellowstone National Park and vicinity with positions of calderas and lava flows. 1, Big Bend Caldera; 2, Henry Forks Caldera; 3, Yellowstone Caldera. Source maps are from Christiansen (1982) and Hildreth *et al.* (1984). Flows in black are low- $\delta^{18}\text{O}$ intra-caldera lavas appearing after formation of Big Bend and Yellowstone calderas; other flows and domes are in speckled pattern. ML and SCR are Mallard and Sour Creek Resurgent Domes. Post Lava Creek Tuff: CF, Canyon Flow; DR, Dunraven Road Flow; NBB, MBB and SBB, North, Middle and South Biscuit Basin Flows, respectively; SCL, Scaup Lake Flow; SL, Summit Lake Flow; WY, West Yellowstone Flow; AC, Aster Creek Flow; SP, Solfatara Plateau Flow; GH, Gibbon Hill Flow; OC, Obsidian Cliff Flow; PH, Paintpot Hill Flow. Post Mesa Falls Tuff: LC, Lewis Canyon Flow; MH, Mount Haynes Flow; HL, Harlequin Lake Flow; GRF, Gardiner River Flow; WRB, Warm River Butte Flow. Post Huckleberry Ridge Tuff: BM, Bishop Mountain Flow; HQ, Headquarters Flow; BC, Blue Creek Flow. BC and HQ originated inside Big Bend caldera but later were truncated by Henry Forks caldera. SRB, Snake River Butte Flow is a pre-HRT flow.

all magmas at Yellowstone makes its isotopic composition particularly diagnostic in inferring the near-liquidus relations in Yellowstone high-silica rhyolites. Zircon is also characterized by slow oxygen diffusion (Valley *et al.*, 1994; Watson & Cherniak, 1997; Peck *et al.*, 1999), sluggish growth relative to common minerals (Watson, 1996), and extremely sluggish cation diffusion (Cherniak *et al.*, 1997a, 1997b). In addition, non-metamict zircon is particularly resistant to secondary hydrothermal alteration of $\delta^{18}\text{O}$ (Gilliam & Valley, 1997) and well known to survive melting episodes (Watson, 1996). Therefore, we use zircon as a 'recorder' of transient changes in $\delta^{18}\text{O}$ of a melt and the source rock, as well as age. The $\delta^{18}\text{O}$ zoning patterns in zircon (and quartz) when combined with knowledge of exchange rates, provide information about the rate and duration of low- $\delta^{18}\text{O}$ magma genesis.

We also present results of a comparative petrologic and mineralogic study of Yellowstone low- $\delta^{18}\text{O}$ and normal- $\delta^{18}\text{O}$ rhyolites which include: whole-rock chemistry; liquidus and zircon saturation temperature estimates; back-scattered electron and cathodoluminescence imaging, and trace element profiling of quartz and zircon grains; and zircon crystal size distribution measurements.

SAMPLE COLLECTION, PREPARATION AND ANALYSIS

Lava and tuff samples were collected using published maps and field guides (Christiansen & Blank, 1972a, 1972b, 1974; Christiansen, 1982, 1989), and were located using maps and the global positioning system (Table 1).

Table 1: Description of rhyolite samples from Yellowstone; ages are from Gansecki et al. ($^{40}\text{Ar}/^{39}\text{Ar}$, 1996, 1998), and Obradovich (K/Ar , 1992); dates are for sanidine or obsidians (where indicated)

Sample	Map unit	Flow/tuff unit	Age, Ar/Ar	Age, K/Ar	Longitude	Latitude	Location
Post Lava Creek Tuff							
YL96-1	Qpcy	West Yellowstone Flow		0.132–0.072, 0.110	110°52'10"	44°29'10"	north cliff
YL96-3	Qpcs	Summit Lake Flow		0.131–0.105, 0.131–0.103	110°52'05"	44°28'42"	Summit Lake trail
YL96-12	Qpca	Aster Creek Flow		0.155, 0.193	110°38'15"	44°15'58"	50 m west of Lewis Falls
YL96-16	Qpcf	Solfatara Plateau Flow		0.108, 0.110	110°37'10"	44°42'10"	Norris Jct, on loop road
YL96-13	Qpm	Mallard Lake Flow		0.149, 0.151	110°43'08"	44°26'35"	above Isa lake, near Craig Pass
YL96-15	Qpo	Paintpot Hill Flow		0.171, 0.183, Obs	110°44'20"	44°41'30"	Paintpot Hill summit
YI96-10	Qpr	Obsidian Cliff Flow		0.171, 0.183, Obs	110°43'40"	44°49'30"	west side on road
YI96-19	Qpoh	Gibbon Hill Dome		0.159, 0.116, 0.148–0.087	110°42'05"	44°42'25"	Gibbon Hill Dome, NE side
YL96-9	Qpul	Scaup Lake Flow	0.198 ± 7	0.226, 0.275	110°48'30"	44°27'10"	west of Old Faithful on loop road
YL96-2	Qpub	South Biscuit Basin Flow			110°52'20"	44°29'08"	north of waterfall of Firehole River
YL96-20	Qpub	Middle Biscuit Basin Flow	0.516 ± 6	0.542	110°49'55"	44°31'38"	bluff across from Excelsior Geyser, roadcut
BBF-1	Qpub	North Biscuit Basin Flow			110°49'25"	44°32'01"	top of 7390 ft hill, Old Faithful–Madison road
YL96-4	Qpud	Dunraven Road Flow	0.486 ± 41	0.672, 0.619–0.680	110°28'00"	44°44'50"	west of Dunraven hill summit
YL96-5	Qpuc	Canyon Flow	0.484 ± 14	0.613, 0.692	110°28'32"	44°44'35"	Canyon campground
YL96-18	Qpuc	Canyon Flow	0.484 ± 14	0.613, 0.692	110°31'12"	44°45'26"	between picnic area and Canyon Jct
CF-1	Qpuc	Canyon Flow	0.484 ± 14	0.613, 0.692	110°28'02"	44°43'12"	Artist Point
<i>Lava Creek Tuff/Yellowstone Caldera</i>			0.602 ± 4				
LCT-3a	Qylau	Member A, upper part		0.641–0.569	110°50'24"	44°39'05"	Tuff Cliffs of Gibbon River, welded
LCT-3a-AI	Qylal	Member A, lower part		0.641–0.569	110°50'24"	44°39'05"	Tuff Cliffs of Gibbon River, single pumice clast
LCT-1	Qylb	Member B		0.673–0.615	111°17'25"	44°08'24"	Mesa Falls Scenic Drive, roadcut
LCT-2	Qylb	Member B		0.641–0.569	111°28'05"	44°16'00"	US20, roadcut
LCT-4	Qylb	Member B		0.641–0.569	110°44'24"	44°42'40"	Mammoth–Canyon roadcut, top of the hill
Post Mesa Falls Tuff							
YL96-7	Qjh	Mt Haynes Flow		0.609, 0.643	110°54'25"	44°38'40"	west of Madison Junction
YL96-8	Qjl	Harlequin Flow		0.840, 0.805	110°53'05"	44°38'40"	east of Harlequin Lake trail
YL96-11	Qlc	Lewis Canyon Flow		0.929–0.965	110°39'18"	44°11'30"	Lewis Canyon cliff, south entrance road
YL96-21	Qlc	Lewis Canyon Flow		0.929–0.965	110°40'15"	44°09'10"	south side of Moose Falls
IP96-2	Qiw	Warm R. Butte Flow		1.13, 1.27	111°14'00"	44°10'10"	east side
<i>Mesa Falls Tuff/Henry Fork Caldera</i>			1.293 ± 12	1.16–1.28			
MFT-1	Qym	Mesa Falls			111°18'38"	44°11'18"	Upper Mesa Falls bluff

We collected samples from all known post-caldera, low- $\delta^{18}\text{O}$ lavas, all units of major tuff eruptions, and other samples covering the 2.0 my eruptive sequence (Table 1).

Individual phenocrysts of quartz and sanidine, and obsidian spheres, were separated from hand specimens

or from crushed rock by hand. Quartz was treated with cold fluoroboric acid to remove adhered feldspars and glass. All analyzed phenocrysts are primary and not the result of secondary precipitation from a hydrothermal fluid. The presence of glass inclusions and igneous morphology were taken as criteria of magmatic origin.

Sample	Map unit	Flow/tuff unit	Age, Ar/Ar	Age, K/Ar	Longitude	Latitude	Location
Post Huckleberry Ridge Tuff							
IP96-1	Qbb	Bishop Mt Flow		1.21, 1.10	110°33'02"	44°19'52"	25 m down from lookout tower
HQ-1	Qbh	Headquarters Flow		1.78, 1.81, 1.86	111°38'53"	44°12'48"	southern pinnacle of the flow
BC-1	Qbf	Blue Creek Flow		1.75, 1.78	111°36'47"	44°13'24"	western slope of the flow
<i>Huckleberry Ridge Tuff /Big Bend Caldera</i>			2.003 \pm 14				
HRT-3a	Qyha	Member A, upper		2.12–1.93	110°43'27"	44°55'55"	Golden Gate Pass, Mammoth–Canyon Hwy
HRT-3a-A2	Qyha	Member A			110°43'22"	44°55'57"	Golden Gate Pass, Mammoth–Canyon Hwy
HRT-1	Qyhb	Member B		2.04–1.99	111°35'38"	44°09'18"	Upper Arcadia Reservoir, north of Ashton
HRT-2	Qyhb	Member B, basal		2.04–1.99	110°43'27"	44°55'55"	Golden Gate Pass, Mammoth–Canyon Hwy
HRT-C	Qyhc	Member C		2.1	110°41'05"	44°00'25"	Lizard Creek, Grand Teton National Park
Pre-Huckleberry Ridge Tuff							
SRB-2	Qysb	Snake River Butte Flow		1.99	111°20'31"	44°07'51"	Snake River Butte, south slope

Zircons were separated from ~ 20 kg rock samples using standard techniques of crushing and density separation, and then purified with cold HF and HNO₃. Separates of 50–250 mg of zircons were further subdivided by sieving into different sizes and by Frantz magnetic separator. No differences in $\delta^{18}\text{O}$ beyond 0.3‰ between different magnetic splits were found. Large-diameter zircons ($>105 \mu\text{m}$, or $>149 \mu\text{m}$) from 15 lavas and tuffs were air abraded in a corundum mortar for 0.5–5 days. Optical measurements, grain counting and mass of the starting vs remaining zircons provide an estimate of the decrease in the average zircon radius. After abrasion, zircons became ellipsoidal to nearly spherical with preferential rounding of pyramids and corners, i.e. along the *c*-axis. This procedure removes mass from zircon in exactly the reverse fashion to the crystal growth, i.e. shortening pyramidal faces grow several times faster than the prismatic faces (Vavra, 1994). Therefore, air abrasion retrieves cores and successive air abrasions provide a retrospective view of $\delta^{18}\text{O}$ during zircon crystallization.

The University of Wisconsin CO₂-laser fluorination–mass-spectrometer system (Valley *et al.*, 1995) provides accurate and precise determination of $\delta^{18}\text{O}$ for individual grains of quartz, sanidine, obsidian spheres and zircon splits. Samples were typically 1–2 mg, yielding 10–30 μmol of CO₂. BrF₅ was used as a reagent. Quartz phenocrysts, often single grains, were analyzed by rapid

heating with defocused laser beam, yielding precise values (better than $\pm 0.1\%$, 1 SD) (Spicuzza *et al.*, 1998a). For analyses of more reactive sanidine and obsidian, an airlock sample chamber was used to prevent partial pre-reaction (Spicuzza *et al.*, 1998b).

Four to seven aliquots of UWG-2 garnet standard were measured at the beginning and end of each analytical session, and sample data were adjusted to the average value of the standards, typically by no more than $\pm 0.2\%$. The average reproducibility of 65 UWG-2 analyses is 0.10‰ (1 SD). Nine NBS-28 quartz analyses yielded an average value of 9.55‰ (Vienna Standard Mean Ocean Water; VSMOW).

Whole-rock chemical analyses for major and trace elements (Rb, Ba, Sr, Y, Nb, Zr) were carried out at XRAL Laboratories (Ontario, Canada) by X-ray fluorescence. The uncertainty of trace element determinations is ± 2 ppm. Mineral and glass major element analyses, and cathodoluminescence imaging were performed on a Cameca SX-50 electron microprobe at the University of Wisconsin. For major element analyses, 15 kV accelerating voltage and 25 nA sample current was used, with synthetic crystals and minerals as standards. For trace element analyses of zircon and quartz, higher voltage (20–25 kV) and sample currents (100–300 nA), and 10–15 min counting times were used (Fournelle *et al.*, 2000). For standards, we analyzed alloys of elements

of interest at high concentrations, and Caltech–Corning synthetic glasses (at low currents) with trace element concentrations of ~ 0.5 – 1 wt %.

Individual zircons in low- $\delta^{18}\text{O}$ rocks were analyzed by Cameca ims-4f ion microprobe at the University of Edinburgh using $^{133}\text{Cs}^+$ primary beam and energy-filtering (Valley *et al.*, 1998a). A homogeneous KIM-5 zircon ($\delta^{18}\text{O} = +5.04\%$, Valley *et al.*, 1998b) with similar Hf content to Yellowstone zircons (0.8–1.2 wt % HfO_2) was used as a standard during the course of analyses. Ion microprobe analyses complement laser fluorination. Laser fluorination gives accuracy of better than $\pm 0.10\%$ (1 SD) for a milligram-size sample, but does not have the capability of analyzing a single zircon (100 $\mu\text{m} \times 200 \mu\text{m}$). Ion microprobe analyses of $\sim 25 \mu\text{m}$ spots can measure zonation in a single zircon crystal, but are less precise ($\sim 1\%$, 1 SD in this study). Laser fluorination of air-abraded zircons was used to precisely measure the composition of zircon cores (in bulk), and the ion microprobe measured the composition of zircon rims and cores for individual crystals.

GEOLOGY AND PETROLOGY OF YELLOWSTONE RHYOLITES

Newly defined low- $\delta^{18}\text{O}$ lava flows

As a result of our fieldwork and oxygen isotope analyses, we propose a subdivision of the low- $\delta^{18}\text{O}$ Biscuit Basin Flow (BBF), which has previously been considered to result from a single eruption. BBF is exposed in three separate outcrops (hills), southern, middle and northern, along the Firehole River of the Upper Geyser Basin (see Fig. 1). These outcrops are separated by sinter and alluvial deposits. Drill hole Y-5 between the southern and middle outcrops does not show the presence of BBF (Christiansen & Blank, 1974). Previous studies analyzed only the middle outcrop across from the Midway Geyser (Hildreth *et al.*, 1984, 1991; Obradovich, 1992; Gansecki *et al.*, 1996). We found that although all three outcrops are equally glassy and rather similar macroscopically, $\delta^{18}\text{O}$ of quartz, zircon, feldspar and obsidian, and mineral–mineral fractionations are dramatically different (discussed below). Petrographically, the southern Biscuit Basin lava (SBB) is characterized by larger and more abundant phenocrysts (17–20 vol. %) than the middle (MBB, 10–12 vol. %), or the northern lava (NBB, 12–15 vol. %). Chemically, the three units are also distinct [Table 2; compare with analyses of Sturchio *et al.* (1986) for SBB and Hildreth *et al.* (1991) for MBB]. We suggest that each hill represents an independent lava flow or extrusive dome. We hence report analyses from all three lavas, calling them North, Middle and South Biscuit Basin Flows.

Petrography

Yellowstone rhyolites are glassy and contain 0–25 vol. % phenocrysts of sanidine, quartz, plagioclase, clinopyroxene, magnetite and apatite, with minor ilmenite, fayalite and orthopyroxene. Zircon is present in all rhyolites. Hydrous minerals are conspicuously absent in all volcanic rocks except member A of the Lava Creek Tuff. Low- $\delta^{18}\text{O}$ and normal- $\delta^{18}\text{O}$ rhyolites contain the same assemblage of phenocrysts, except for post-LCT low- $\delta^{18}\text{O}$ lavas, which are poorer in quartz and richer in plagioclase (oligoclase) at the expense of sanidine. Plagioclase is characterized by a sieved texture and optically shows complex zoning.

Quartz in low- $\delta^{18}\text{O}$ lavas often has a corroded morphology and smaller grain sizes than in normal- $\delta^{18}\text{O}$ lavas (Fig. 2), especially in the glassy Canyon and Dunraven Road flows, where the quartz grain size is < 0.5 mm and the concentration is < 0.5 vol. %. Quartz is more abundant (~ 1 – 2 vol. %, 1 mm) in the Biscuit Basin Flows (post-LCT) and Blue Creek Flow (post-HRT).

Cathodoluminescence (CL) imaging of quartz phenocrysts by electron microprobe from low- $\delta^{18}\text{O}$ and normal- $\delta^{18}\text{O}$ rhyolites revealed morphological features indicative of multiple episodes of magmatic dissolution–reprecipitation. Elongated melt inclusions penetrate the interior of quartz grains, truncating growth zones (Fig. 2a). Concentric growth is recorded in other quartz phenocrysts. Many quartz phenocrysts exhibit a bright core surrounded by a dark rim by CL. Trace element profiling by electron microprobe through one quartz crystal in South Biscuit Basin Flow (Fig. 2b) indicates that brighter zones and layers are richer in Al and K (up to 0.08 wt %). Al is proposed to cause bright CL in quartz (Marshall, 1988). No definite correlation between $\delta^{18}\text{O}$ of quartz and its CL pattern was found. Secondary, hydrothermally precipitated quartz sporadically occurs in altered lavas. Precipitated quartz is distinguished from phenocrysts by perfectly faceted, elongated, singly terminated prismatic crystals, and the absence of melt inclusions. No healed cracks, observed elsewhere in hydrothermally altered quartz (Valley & Graham, 1996; King *et al.*, 1997), were found at Yellowstone.

Zircon is ubiquitous in all rhyolites of Yellowstone and provides the most compelling constraints in interpreting petrogenesis (see Appendix). Careful examination of mineral separates revealed that some zircons are included in sanidine, quartz and magnetite phenocrysts. HF dissolution of both magnetite and sanidine + quartz separates yielded many tens of grains of zircon, indicating that zircons were located inside these minerals and pre-date crystallization of sanidine, quartz and magnetite. In particular, up to a third of all extracted zircons resided in magnetite in units CF and DR. This conclusion is in accordance with high zircon saturation temperatures

Table 2: Whole-rock analyses of rhyolitic lava flows and tuffs and the major element composition of melt inclusions in quartz

Sample	SiO ₂ (wt %)	TiO ₂ (wt %)	Al ₂ O ₃ (wt %)	Fe ₂ O ₃ (wt %)	MgO (wt %)	MnO (wt %)	CaO (wt %)	Na ₂ O (wt %)	K ₂ O (wt %)	P ₂ O ₅ (wt %)	LOI (wt %)	Sum (wt %)	Rb (ppm)	Sr (ppm)	Y (ppm)	Zr (ppm)	Nb (ppm)	Ba (ppm)	Zr _{sat} (°C)	Liq. T (°C)	
<i>Extracaldera</i>																					
YL96-10	76.6	0.083	11.90	1.57	0.02	0.02	0.51	3.58	4.62	0.03	0.30	99.3	229	6	77	192	49	36	805	849	
YL96-15	77.6	0.067	12.00	1.75	<0.01	0.02	0.21	3.79	4.16	0.03	0.50	100.2	226	3	45	202	60	29	818	840	
YL96-19	77.1	0.048	12.10	1.52	<0.01	0.02	0.32	3.84	3.98	0.03	0.60	99.7	298	<2	65	189	102	<20	812	838	
<i>Postcaldera-intracaldera</i>																					
YL96-2*	75.3	0.246	12.60	2.06	0.15	0.04	0.87	3.27	4.75	0.05	0.55	100.2	159	67	56	315	51	1100	854	850	
BBF-1	74.9	0.168	12.00	1.56	0.03	0.03	0.43	3.21	5.19	0.01	0.60	98.2	188	20	44	248	48	326	831	856	
YL96-20*	77.4	0.118	11.30	1.70	0.03	0.03	0.43	2.97	4.57	0.04	0.45	99.2	189	21	46	204	47	286	819	826	
YL96-4*	75.7	0.289	12.40	2.42	0.11	0.06	0.85	3.28	4.13	0.05	0.95	100.5	130	78	55	393	73	956	882	829	
YL96-5*	72.7	0.116	11.50	1.28	0.03	0.03	0.53	3.92	4.70	0.03	0.60	98.6	169	18	49	211	42	611	854	851	
YL96-18*	76.2	0.118	11.80	1.55	<0.01	0.03	0.40	3.22	4.83	0.04	0.45	98.8	160	21	33	225	40	657	825	845	
CF-1	77.1	0.277	12.40	0.43	0.05	<0.01	0.09	0.02	0.09	0.05	4.65	95.3	<2	106	19	316	49	434	975		
YL96-9*	74.8	0.253	12.30	2.09	0.11	0.11	0.78	3.13	4.72	0.05	0.60	99.1	158	61	39	312	51	1060	855	847	
YL96-1	79.0	0.137	10.70	1.88	<0.01	0.04	0.47	3.08	4.42	0.03	0.25	100.1	162	10	64	296	50	164	849	818	
YL96-3	76.8	0.132	11.60	1.93	0.01	0.04	0.48	3.34	4.80	0.03	0.40	99.6	179	6	76	300	60	126	848	845	
YL96-12	76.8	0.159	11.80	1.68	0.04	0.03	0.45	3.18	4.83	0.04	0.40	99.5	175	19	43	266	58	325	841	843	
YL96-16	75.0	0.210	11.70	2.75	<0.01	0.06	0.74	3.45	4.59	0.03	0.30	99.0	122	12	75	549	63	870	905	846	
YL96-13	75.9	0.158	11.70	1.72	<0.01	0.03	0.39	3.17	4.90	0.04	0.45	98.6	174	18	52	264	53	335	839	846	
<i>Lava Creek Tuff</i>																					
LCT-2B	73.8	0.160	12.20	1.92	0.06	0.04	0.42	3.39	5.44	0.02	0.55	98.2	182	18	43	365	62	386	863	872	
LCT-3A	78.1	0.101	11.20	1.39	0.03	0.02	0.35	3.25	4.34	<0.01	0.10	99.0	199	10	68	185	49	129	809	825	
<i>Post Mesa Falls Tuff</i>																					
YL96-8	76.6	0.178	12.20	2.09	0.09	0.05	0.48	3.04	4.71	0.05	0.60	100.2	168	35	68	312	56	652	862	838	
YL96-7	77.4	0.115	11.90	1.60	0.05	0.02	0.36	3.30	4.73	0.03	0.30	99.9	236	6	52	194	64	65	813	843	
YL96-11	75.3	0.207	12.60	2.37	0.06	0.05	0.75	3.39	4.37	0.05	1.00	100.3	138	62	47	379	53	917	877	843	
YL96-21	76.2	0.255	12.00	1.91	0.03	0.02	0.61	3.15	4.86	0.06	0.45	99.8	176	53	41	325	55	824	859	844	
IP96-2	76.8	0.078	12.70	1.46	<0.01	0.03	0.44	3.49	4.24	0.04	0.95	100.4	255	5	48	153	80	37	797	840	
<i>Mesa Falls Tuff</i>																					
MFT-2	77.6	0.123	11.40	1.44	0.04	0.02	0.36	2.96	4.89	0.01	0.55	99.5	222	17	42	168	40	195	800	834	
<i>Post-Huckleberry Ridge Tuff</i>																					
IP96-1	76.9	0.127	12.30	2.00	<0.01	0.08	0.45	3.44	4.51	0.03	0.25	100.3	177	7	55	270	75	135	845	843	
BC-1*	75.5	0.197	11.70	2.24	0.01	0.04	0.34	3.37	4.89	0.02	0.25	98.8	175	34	48	394	41	1170	876	851	
HQ-1*	74.8	0.181	11.80	2.16	0.03	0.04	0.41	3.46	4.94	0.03	0.40	98.5	190	25	74	388	44	947	872	856	
<i>Huckleberry Ridge Tuff</i>																					
HRT-C	75.6	0.213	11.80	3.51	0.03	0.07	0.51	3.39	4.01	0.02	0.50	99.1	150	106	54	445	28	1780	897	827	
HRT-1B	73.6	0.213	13.27	2.69	0.06	0.05	0.86	3.73	5.30	0.03	0.26	100.3	118	53	69	399	42	1640	868	874	
HRT-3a	77.3	0.152	12.60	1.27	<0.01	0.02	0.75	3.40	4.37	0.01	0.40	100.4	151	38	70	328	53	973	863	841	
<i>Pre-Huckleberry Ridge Tuff</i>																					
SRB	75.2	0.176	12.10	1.97	0.06	0.03	1.37	3.05	5.04	0.05	1.05	100.2	176	48	65	285	42	588	831	803	
<i>Melt inclusions in quartz</i>																					
YL96-4*	76.0	0.20	12.71	1.30	0.05	0.50	0.50	3.30	5.90			100.0								865	
YL96-12	74.6	0.20	13.98	1.18	0.04	0.55	3.09	3.64	6.32			100.0								880	
IP96-1	76.9	0.07	12.77	0.90	0.01	0.38	3.64	5.36				100.0								869	

See Table 1 for sample description and abbreviations. Zr_{sat}, T, zircon saturation temperature (e.g. Watson & Harrison, 1983); Liq. T, liquidus temperature at 3 wt % water (IMELTS, Ghiorso & Sack, 1995).

*Low- $\delta^{18}\text{O}$ samples.

YL96-2

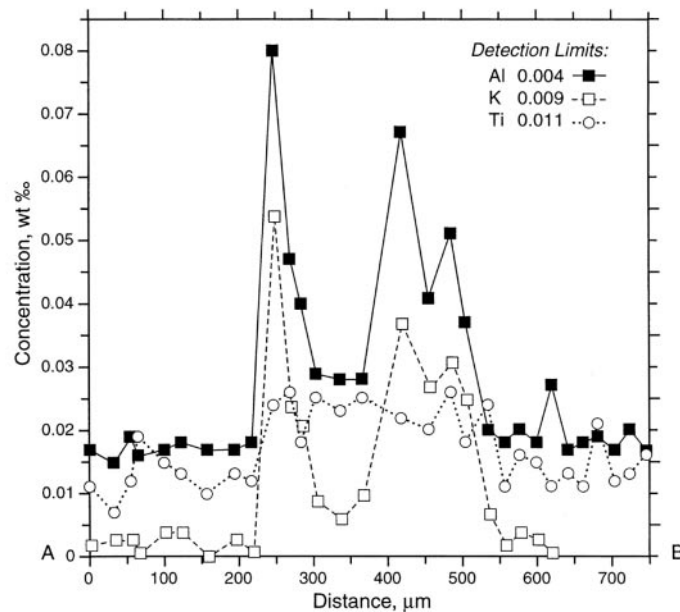
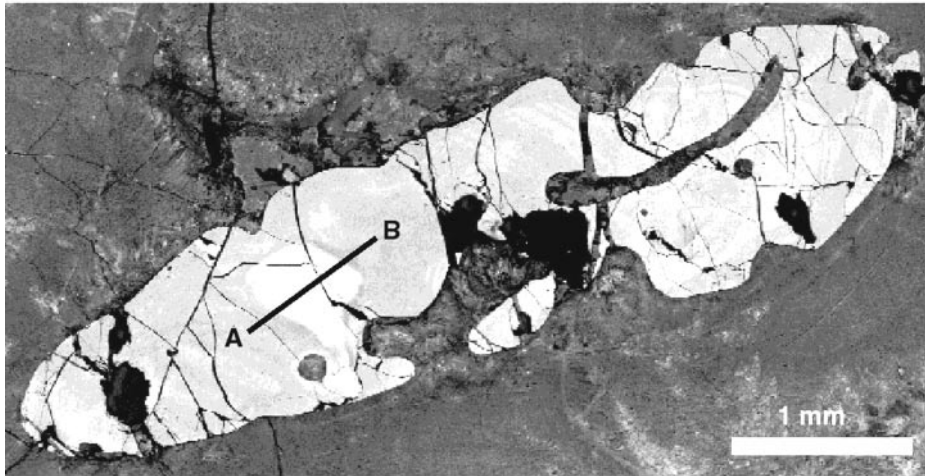


Fig. 2. Cathodoluminescence image of quartz in rhyolite from the South Biscuit Basin Flow and trace element profile through its core along line A-B. Inclusions are devitrified glass. Hourglass elongated melt inclusions are explained by Marangoni convection, gas bubble 'drilling' as a result of surface tension effects (Donaldson & Henderson, 1988), and are a resorption feature.

(800–910°C; see Table 2), confirming that zircon is a near-liquidus phase, and that almost all Yellowstone magmas were always saturated with respect to zircon.

SEM examination of zircon grain mounts revealed grains of chevkinite (units SBB, DR) and baddeleyite (CF). Baddeleyite forms euhedral prismatic crystals of up to 100 μm long and contains 1–2 wt % of HfO₂ and TiO₂, and 3 wt % of Nb₂O₅. The presence of baddeleyite in high-silica rhyolite is remarkable and has not been reported previously. Typically occurring in silica-undersaturated rocks, baddeleyite can be present in direct contact with quartz in late-stage silica-rich differentiates

of mafic plutons (Heaman & LeCheminant, 1993), although it is not thermodynamically stable with quartz below 1676°C.

Whole-rock chemistry

Low-δ¹⁸O rhyolites of each eruptive cycle are chemically similar to normal-δ¹⁸O lavas (Table 2). In addition, whole-rock compositions are similar in major element chemistry to melt inclusions in quartz, determined by electron microprobe analysis (see Table 2). This similarity

indicates lack of secondary alteration of volcanic glass, such as alkali removal, in fresh-looking glassy samples.

The comparison of low- $\delta^{18}\text{O}$ and normal- $\delta^{18}\text{O}$ rhyolites was carried out using Sr/Rb and Ba/Rb ratios, which provide a measure of differentiation in similar high-silica rhyolites elsewhere (e.g. Anderson *et al.*, 2000). For example, earlier erupted members of Huckleberry Ridge Tuff and Lava Creek Tuff are more differentiated based on lower Sr and Ba (down to a few ppm), higher Rb, and lower Sr/Rb ratios (Fig. 3a). We stress here that Sr/Rb and Ba/Rb ratios are also vulnerable to change by hydrothermal fluids, as glass-hosted Rb is more soluble than mostly feldspar-hosted Ba and Sr. Ratios of fluid-immobile elements to alkalis, such as Zr/Rb, are another measure of alkali loss during hydrothermal alteration (Fig. 3b). An example of this is the pervasively altered sample of Canyon Flow (CF-1, Table 2), collected at Artist Point of Yellowstone Canyon, which contains virtually no Na, K and Rb, whereas other major and trace elements are undisturbed. It should be noted that concentrations of fluid-insoluble Zr are nearly identical in this hydrothermally altered sample to those in low- $\delta^{18}\text{O}$ rhyolites or normal rhyolites, demonstrating the immobility of Zr (and zircon) in the course of ^{18}O depletion. Even hot, acidic fluids have been shown not to disturb Zr in volcanic rocks (Terakado & Fujitani, 1998).

We find neither clear chemical differences between low- $\delta^{18}\text{O}$ and normal- $\delta^{18}\text{O}$ rhyolites, nor evidence of preferential leaching of major or trace alkalis. On the contrary, low- $\delta^{18}\text{O}$ rhyolites roughly follow differentiation trends defined by normal rhyolites with scatter that can be explained by local and regional source rock heterogeneities (Fig. 3a and b). Most ^{18}O -depleted, post-LCT rhyolites contain slightly more Mg, Sr and Ba, and less SiO_2 and Rb. Therefore, they are slightly more 'primitive' than normal- $\delta^{18}\text{O}$ post-LCT rhyolites. The relations are opposite for post-HRT low- $\delta^{18}\text{O}$ rhyolites, which are slightly more evolved than HRT and later lavas. More significantly, low- $\delta^{18}\text{O}$ rhyolites of the last eruptive cycle (post-LCT) display a large, within-cycle diversity (Fig. 3), suggesting that they do not represent a single well-mixed melt.

The similar major element composition of low- $\delta^{18}\text{O}$ rhyolites vs normal- $\delta^{18}\text{O}$ rhyolites (Table 2) may indicate that hydrothermal fluids were saturated with respect to alkalis and other soluble trace elements, and did not quantitatively remove these elements from the magma generation zones before melting. The preservation of trace element concentrations comes as no surprise, as these hydrothermal fluids consist of 88% oxygen and only parts per million of trace elements (e.g. Lewis *et al.*, 1997). Thus, for moderate fluid/rock ratios of 0.5–1, oxygen in a rock is diluted by over 10%, but trace elements are not measurably affected. In such an environment, oxygen isotopes are decoupled from trace

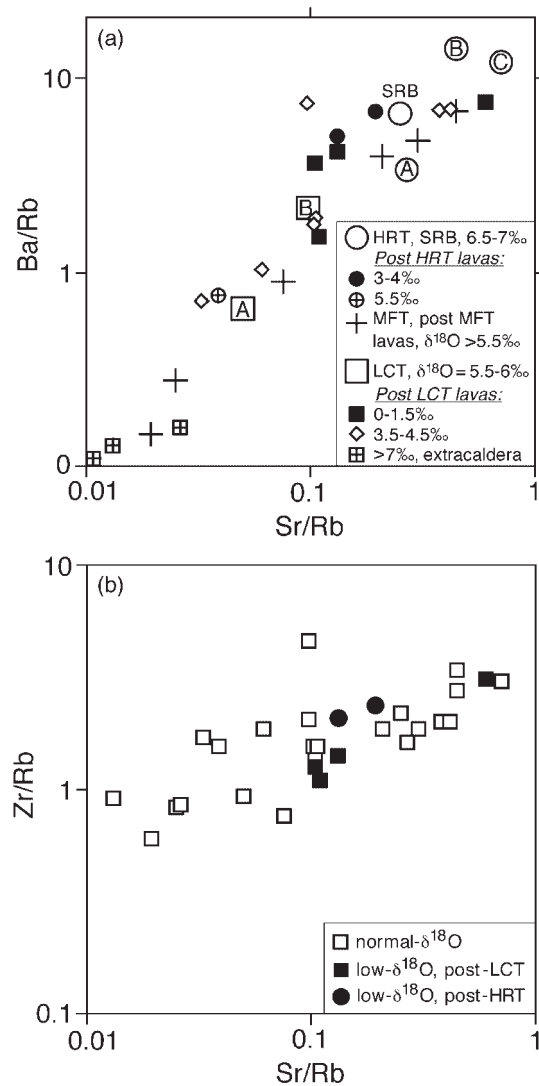


Fig. 3. Ba/Rb vs Sr/Rb (a), and Zr/Rb vs Sr/Rb (b) diagrams for lavas and tuffs (whole rocks) of Yellowstone; data are from Table 2. These correlations are interpreted to mostly result from fractional crystallization, as Sr and Ba are preferentially removed with feldspars, and Zr with zircon. Hydrothermal alteration would produce unusually high ratios of insoluble Zr to soluble Rb, which are not seen. It should be noted that low- $\delta^{18}\text{O}$ lavas fall onto this differentiation trend independent of $\delta^{18}\text{O}$ value. Abbreviations are unit names from Fig. 1. A, B in square boxes are members of LCT; A, B, and C in circles are members of HRT.

elements and meteoric water is capable of significantly changing $\delta^{18}\text{O}$, but not cations.

Liquidus temperatures of magmas

Temperature estimates for zircon saturation (Watson & Harrison, 1983) vary from 830 to 910°C for the three major tuff eruptions and are similar to those for low- $\delta^{18}\text{O}$ intra-caldera rhyolites (800–875°C; see Table 2).

Magnetite–ilmenite thermometry yields 820–920°C, and oxygen fugacities close to quartz–fayalite–magnetite (QFM) buffer (Hildreth *et al.*, 1984). Neither method indicates a significant temperature difference between low- $\delta^{18}\text{O}$ and normal- $\delta^{18}\text{O}$ magmas, with the exception that the low- $\delta^{18}\text{O}$ rocks are slightly more oxidized and plot 0.5 log unit above the QFM buffer (Hildreth *et al.*, 1984). The bulk chemical compositions, plotted on an Ab–Or–Qz diagram, point to a relatively water-poor composition ($PH_2O < 0.5$ kbar), shallow crustal pressures (0.5–2.5 kbar), and high temperatures (850–950°C) for Yellowstone rhyolite magmas (e.g. Doe *et al.*, 1982).

Liquidus and solidus temperatures were also determined using the MELTS program (Ghiorso & Sack, 1995) based on whole-rock analyses and the composition of melt inclusions (see Table 2). We found no difference in calculated liquidus or solidus temperatures between low- $\delta^{18}\text{O}$ and normal- $\delta^{18}\text{O}$ rhyolites resulting from similar major element chemistry. At 3 wt % H_2O and 1 kbar, the calculated liquidus temperatures are similar to zircon saturation temperatures with the average at 850°C (see Table 2). For these conditions, the minimum solidus temperatures, or eutectic, are between 710 and 750°C. A rise from 710 to 750°C leads to a spontaneous increase in melt fraction from 0% to >50%. This increase plays an important role in the segregation of rhyolite magmas, discussed below. These liquidus–solidus relations are consistent with melting–crystallization experiments with similar high-silica rhyolitic compositions (Whitney, 1988).

OXYGEN ISOTOPE RESULTS

Oxygen isotope ratios of minerals and glass from 25 eruptive units of Yellowstone are listed in Table 3. In Fig. 4, $\delta^{18}\text{O}$ is plotted against the age of each eruptive unit (see Table 1). Each sample is represented by the vertical line on which $\delta^{18}\text{O}$ of coexisting minerals is plotted allowing visual estimation of mineral variability and mineral–mineral isotopic fractionation.

General observations

Individual quartz phenocrysts

Individual quartz phenocrysts (Fig. 4a) show an evolution pattern with extreme $\delta^{18}\text{O}$ depletions after LCT and HRT eruptions. This pattern follows the trend of bulk phenocrysts shown by Hildreth *et al.* (1984) with one important difference. Analyses of individual quartz phenocrysts reveal strong variability from grain to grain in low- $\delta^{18}\text{O}$ rhyolites which erupted immediately after the LCT, with 1–2‰ variations among different crystals within a single hand specimen. This variability exceeds 2‰ for Canyon Flow and South Biscuit Basin Flow (Fig.

4a and b). Post-HRT low- $\delta^{18}\text{O}$ rhyolites also show $\delta^{18}\text{O}$ variability among quartz phenocrysts. In contrast, analyses of individual quartz phenocrysts from other rhyolites are homogeneous to within $\pm 0.2\%$. Thus, many quartz phenocrysts in the low- $\delta^{18}\text{O}$ rocks are not in equilibrium with each other, the host obsidian or feldspar. Values of $\Delta^{18}\text{O}(\text{Qz–Obs})$ and $\Delta^{18}\text{O}(\text{Qz–Fsp})$ are larger than equilibrium values of 0.35‰ and 0.75‰ for magmatic temperatures (see below, Table 3) and many quartz phenocrysts have higher than equilibrium $\delta^{18}\text{O}$ values. There is no correlation between crystal size and $\delta^{18}\text{O}$.

Zircon

Oxygen isotope ratios of zircon broadly follow the quartz trend (Fig. 4a and b). $\Delta^{18}\text{O}(\text{Qz–Zrc})$ are in high- T equilibrium for normal- $\delta^{18}\text{O}$ pre-caldera and extra-caldera lavas and tuffs, and $\delta^{18}\text{O}$ of different size fractions of zircon are on average homogeneous within $\pm 0.15\%$ (1 SD). In contrast, low- $\delta^{18}\text{O}$ lavas are characterized by zircon–quartz disequilibrium (Fig. 4c and d; Table 3). Values of $\Delta^{18}\text{O}(\text{Qz–Zrc})$ between individual quartz phenocrysts and bulk separates of zircon deviate by >2‰ below the equilibrium value of $2.19 \pm 0.07\%$ (Fig. 4d). Values of $\Delta^{18}\text{O}(\text{Obs–Zrc})$ and $\Delta^{18}\text{O}(\text{Fsp–Zrc})$ are often less than 1.76‰ and 1.45‰, respectively. Thus, zircon is ^{18}O richer than expected for equilibrium with quartz at magmatic temperatures. In addition, differences of up to 0.7‰ in $\delta^{18}\text{O}$ exist between the smallest (<53 μm diameter) and largest (>149 μm) zircons from all low- $\delta^{18}\text{O}$ lava flows erupted after LCT, and in Blue Creek Flow erupted after HRT.

Individual obsidian spheres and feldspar phenocrysts

Analyses of sanidine phenocrysts (and their parts) and obsidian spheres demonstrate that sanidine is a fraction of a per mil lower in $\delta^{18}\text{O}$ than obsidian, and obsidian is a fraction of a per mil lower than quartz. These fractionations are characteristic of equilibrium at magmatic temperatures for silicic rocks (e.g. Taylor & Sheppard, 1986). In low- $\delta^{18}\text{O}$ lavas of the post-LCT cycle, $\delta^{18}\text{O}$ values of plagioclase (andesine) overlap with the $\delta^{18}\text{O}$ range of obsidian, confirming that their magmatic $\delta^{18}\text{O}$ values were not hydrothermally altered following emplacement. Furthermore, analyses of individual sanidine phenocrysts and obsidian spheres in low- $\delta^{18}\text{O}$ lavas that show heterogeneity among individual quartz phenocrysts, demonstrate remarkable homogeneity (Table 3).

Mineral–mineral and mineral–obsidian fractionations

With the exception of low- $\delta^{18}\text{O}$ lavas appearing after LCT and HRT, all other rocks exhibit similar, small and regular isotopic mineral–mineral, and mineral–obsidian fractionations, consistent with magmatic temperatures. All lavas in this study are high-silica rhyolites and have

Table 3: Oxygen isotope composition of minerals and glass of Yellowstone Plateau volcanic field

Sample	$\delta^{18}\text{O}$	Sample	$\delta^{18}\text{O}$	Sample	$\delta^{18}\text{O}$	Sample	$\delta^{18}\text{O}$
SRB-2	SRB	HQ-1	HQ	YL96-21	LC	LCT-1B	LCT-B
Qz, md	7.49	Qz, sm	4.23	Qz, bg	6.92	Qz, bg	6.45
Qz, md	7.21	Qz, sm	4.30	Qz, sm	6.05	Qz, bg	6.54
Qz, md	7.30	Qz, md	4.15	Qz, md	6.36	Qz, bg	6.46
San-1	6.54	Qz, bg	3.96	Qz, bg	6.81	Qz, bg	6.25
San-2	6.54	Qz, bg	4.01	Zrc, 5NM	4.20	San, bulk	5.49
		Zrc, <149, 37% abr	2.08	Zrc, 15M	4.33		
HRT-3a-A2	HRT-A	Zrc, <53	1.89	Zrc, 5M	3.97	YL96-20	MBB
Qz, ind	7.38	Zrc, <53	1.91	Obs	6.18	Qz, sm	1.06
Qz, bg	7.70	San-1	3.23			Qz, 2 sm	0.88
Qz, bg	7.50			YL96-8	HL	Qz, sm	0.87
		IP96-1	BM	Qz, bg, rim-1	6.59	Qz, many sm	1.36
HRT-3a	HRT-A	Qz, ind	6.04	Qz, bg, rim-2	6.41	Qz, 4 sm	0.89
Qz, bg	7.47	Qz, ind	5.42	Qz, bg	5.90	5M	0.49
Qz, bg	7.22	Qz, ind	5.60	Qz, bg	6.03	5NM	0.48
Qz, md	7.41	Qz, ind	5.94	5NM	3.60	Zrc, >149	1.11
Qz, bg	7.16	Zrc, <53, 5NM	3.91	15M	3.98	Zrc, <53	0.29
		Zrc, >149, 5NM	3.84	10M	3.92	Zrc, >105, 15% abr	1.73
HRT-1	HRT-B	San-1-1	5.56	Zrc, >149, 25% abr	4.38	Zrc, >105, 37% abr	1.89
Qz, sm	8.13	San-1-2	5.32	Zrc, <53	3.71	Zrc, <53, 5NM	0.43
Qz, md	7.39	Obs	5.55	San, big	5.28	Zrc, >105, 50% abr	2.80
Qz, bg	6.61					Pl-1	1.60
Qz, ind	7.58	MFT-2	MFT	YL96-7	MH	Obs	0.79
Zrc, bulk	5.17	Qz, ind	6.02	Qz, ind	6.78	Obs-1	1.18
Zrc, <53	5.14	Qz, bg	5.70	Qz, md	6.45	Obs-2	1.37
Zrc, >149	5.34	Qz, md	6.01	Qz, md	6.47		
San, bulk	6.33	Qz, md	6.10	Qz, ind	6.26	BBF-1	NBB
		Qz, bg	6.07	Qz, ind	6.50	Qz, md	4.80
		Zrc, bulk	3.62	Qz, bg	6.18	Qz, md	4.41
HRT-2	HRT-B	Zrc, <53	3.57	Zrc, bulk-1	3.97	Qz, bg	4.81
Qz, md	7.98	Zrc, >105	3.67	Zrc, bulk-2	3.84	Qz, md	4.69
Qz, sm	7.04			Obs	6.67	Qz, bg	4.52
Qz, md	7.24	IP96-2	WRB			Zrc, bulk	2.56
Qz, md	7.16	Qz, ind	5.02	LCT3a, A1	LCT-A	Zrc, <53	2.72
		Qz, bg	5.32	Qz, ind	6.12	Zrc, >105	2.47
HRT-C	HRT-C	Qz, bg	5.69	Qz, ind	6.22	Zrc, >105, 19% abr	2.53
Qz, md	8.04	Zrc, >149, 20% abr	3.89			Zrc, >105, 19% abr	2.60
Qz, bg	8.25	Zrc, <53	3.52	LCT3a	LCT-A	Obs	4.18
Qz, md	7.93	5NM	3.58	Qz, md	6.79		
Qz, md	7.60	San-1	4.92	Qz, bg	6.48	YL96-5	TSC/CF
Zrc, bulk	5.57	San-2	5.05	Qz, bg	6.51	Qz, ind	1.27
Zrc, <53	5.78			Qz, sm	6.61	Qz, ind	0.83
Zrc, >149	5.62	YL96-11	LC	Zrc, <53	4.15	bulk	1.22
		Qz, ind	6.38	Zrc, >149	4.12	Qz, bg	1.27
BC-1	BC	Qz, ind	6.62	Zrc, bulk	4.16	Qz, ind	1.91
Qz, bg-1	3.67	Qz, ind-1	6.00	San, bulk	5.34	Qz, sm	1.87
Qz, bg-2	3.29	Qz, ind-1	6.01			Obs	0.32
Qz, bg-3	3.97	Zrc, >149, 15M	4.04	LCT-2, B	LCT-B		
Qz, bg-4	3.57	Zrc, <53, 15M	4.18	Qz, bg	6.18	CF-2	CF
Qz, md	3.99	5NM	4.18	Qz, bg	6.63	Obs-1	1.15
Qz, ind	3.71	San, md	5.98	Qz, md	6.36		
Zrc, >105, 36% abr	2.47	San, bg	5.85	Qz, sm	6.30		
Zrc, >105, 23% abr	2.02						
Zrc, >105, 23% abr	2.07						
Zrc, <53	1.46						
Zrc, bulk	1.62						
San-1	2.94						

Table 3: continued

Sample	$\delta^{18}\text{O}$	Sample	$\delta^{18}\text{O}$	Sample	$\delta^{18}\text{O}$	Sample	$\delta^{18}\text{O}$
YL96-18	CF	YL96-2	SBB	YL96-16	SP	YL96-9	SCL
Qz, ind	1.48	Qz, bg	4.35	Qz, md	3.73	4 Qz, sm	4.45
Qz, 3 sm	4.71	Qz, sm,<1 mm	4.60	Qz, md	3.30	Qz, bg	4.45
Qz, 5 sm	1.46	Qz, md, 1 mm	4.56	Qz, ind	3.24	Qz, ind	4.50
Qz, 3 sm	3.42	Qz, bg, platy	5.66	Qz, sm	3.77	Qz, ind	4.27
Qz, 3 sm	3.63	Qz, bg	5.77	Qz, bg	3.96	Zrc, 5M	1.54
Qz, 4 sm	1.66	Qz, ind	3.53	Zrc, 10M	2.02	Zrc, <53, 15M	1.46
Zrc, 5NM	3.22	Qz, ind	4.56	Zrc, 5NM	2.06	Zrc, >149, 15M	1.41
Zrc, 5M	3.76	Qz, bg	4.29	Zrc, in Mt	2.11	Zrc, <53, 15M	1.69
Zrc, 5M	3.61	Qz, bg	4.16	San-1	2.88	Zrc, >149, 24% abr	1.27
Zrc, >105, 30% abr	3.74	Qz, md-2, bulk	4.36	San-2	3.03	Obs	4.02
Zrc, <74	2.04	Qz, bg-6, rim	5.80	San-3	2.81		
		Qz, bg-6, core	5.85	Obs	3.23	YL96-13	ML
YL96-4	DR	Qz, bg-6, core	5.90	YL96-10	OC	Qz, sm	4.34
Qz, md	1.99	Qz, bg-6, rim	5.80	Qz, bulk	7.08	Qz, ind	4.61
Qz, md	1.63	Qz, md	5.03	Qz, sm	7.40	Qz, sm	4.50
Qz, md	1.43	Qz, md, core	4.21	Zrc, 5M	5.53	Zrc, 5NM	2.48
Qz, sm	1.79	Qz, bg	6.19	Zrc, 15M	5.24	Zrc, 5NM	2.45
Qz, bg	1.63	Qz, bg	6.20	Obs	6.93	Zrc, <53, 5NM	2.63
Qz, ind	1.89	Qz, sm	5.11	YL96-19	GH	Zrc, >149, 28% abr	2.80
Qz, ind	1.32	Qz, 3 sm	5.33	Qz, bg	7.93	Obs	4.57
Qz, ind	1.40	Qz, sm	5.64	Qz, ind	7.49	YL96-1	WY
Qz, ind	1.03	Qz, 2 sm	5.44	Qz, ind	7.52	Qz, ind	5.14
Zrc, >53<149	0.15	Qz, md	5.53	Qz, bg, core-1	7.47	Qz, ind	5.01
Zrc, <53	-0.40	Qz, md	5.48	Qz, bg, core-2	7.61	Qz, bg	5.21
Zrc, <53, 5NM	-0.12	Qz, md, rim	4.18	Zrc, 5NM	4.80	Qz, md	5.34
Zrc, >53<105	-0.02	Qz, bg, core	4.31	Zrc, 5M	4.97	Qz, bg	4.98
Zrc,<53	-0.17	Qz, bg, rim	4.50	Fsp, bulk	7.24	Zrc, 15M	2.65
Zrc, >105, 25% abr	1.84	Zrc, >149, 5NM	1.57	YL96-15	PH	Zrc, 5M	2.83
Zrc, >105, 25% abr	1.78	Zrc, >149, 37% abr	3.54	Qz, ind	7.95	Zrc, >105, 32% abr	2.76
San-1	0.61	Zrc, >53, 5NM	1.72	Qz, ind	7.38	San-1	4.06
Obs-1	1.07	Zrc, <53, 5NM	1.73	Qz, ind	7.03	San-2	4.46
Obs-2	0.88	Zrc in Mt	1.31	Qz, ind	7.91	YL96-12	AC
Obs-3,4	1.10	Zrc in Fsp and Qz	1.61	Qz, 2 sm	7.38	Qz, bg	4.88
Obs-5	1.09	San-7-1	3.49	Qz, ind	7.86	Qz, 5 sm	4.99
YL96-3	SL	San-7-2	3.53	Zrc, 5NM	4.97	Qz, ind	4.65
Qz, bg	4.80	San-6	3.56	Zrc, 5M	5.10	Qz, ind	4.85
Qz, bg	4.90	San-5	3.61	San-1	6.82	Zrc, 15M	3.17
Qz, ind	4.88	San-5-bis	3.62	San, bulk	6.57	Zrc, 15M	2.90
Zrc, bulk-1	2.67	San-1	3.73			Zrc, 5NM	2.88
Zrc, bulk-2	2.40	San-8	3.62			Zrc, <53, 15 M	2.52
San, bg	4.36	Obs-5	3.74			Zrc, >149, 40% abr	2.95
		Obs-4	3.86			San, bg	3.96
		Obs-3	3.86				
		Obs-2	3.56				
		Obs-1	3.58				

<53, >79, >105, >149 (μm) are zircon size fractions (diameter); 5NM, 5M, 10M, 15M are magnetic fractions of zircon; magnetism increases from 5NM (nonmagnetic) to 15M (most magnetic); 37% is 37 vol. % abraded zircon cores (63% remaining); sm, md, bg are small, medium, big crystals in each rock; ind is an individual crystal, bg-2 is a crystal number, San-7-2 is part of the San-7 crystal, 2 sm is an analysis made of two small crystals; bulk indicates many crystals without subdividing into size or magnetic fractions.

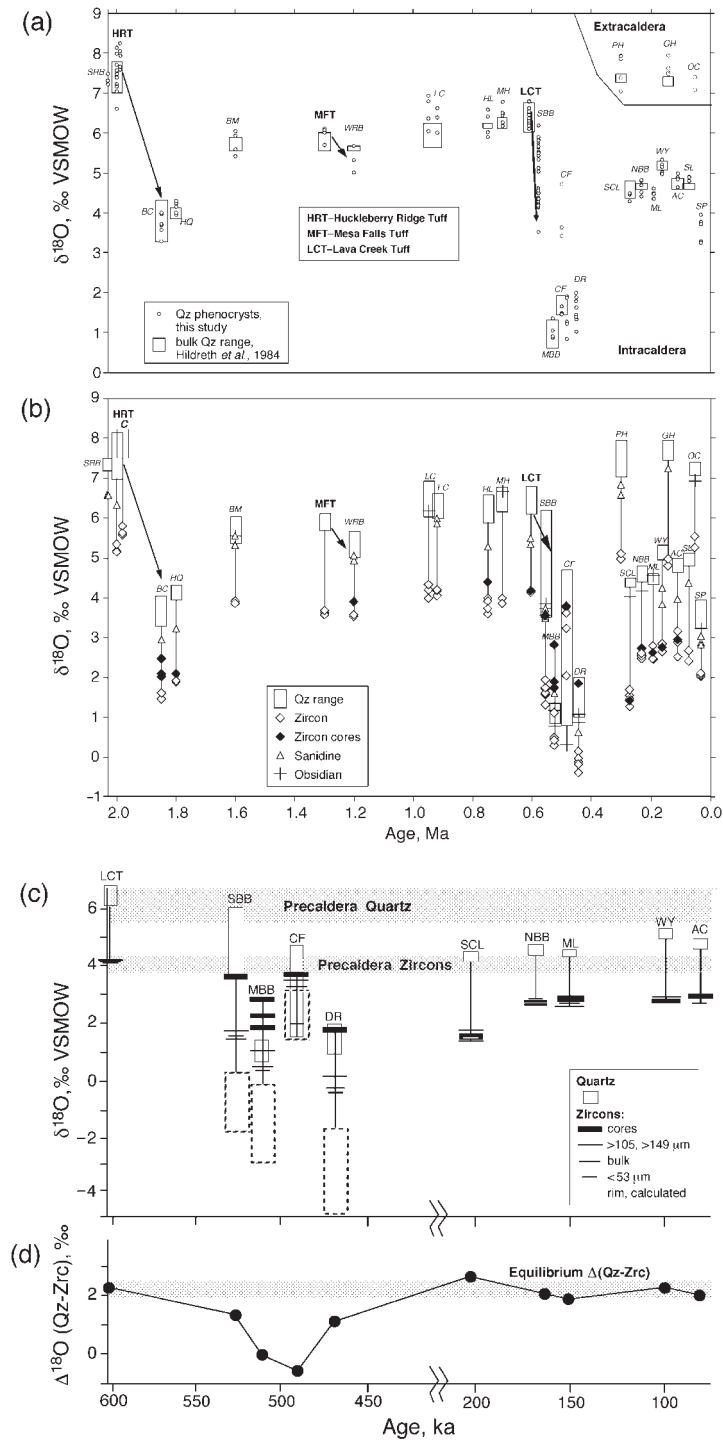


Fig. 4. Oxygen isotope evolution of Yellowstone magmas. Values of $\delta^{18}\text{O}$ and unit names are from Table 3 and Fig. 1. Major climactic eruptions are Huckleberry Ridge Tuff (HRT), Mesa Falls Tuff (MFT), and Lava Creek Tuff (LCT). Ages are from Obradovich (1992, K/Ar) and Gansecki *et al.*, (1996, 1998, $^{40}\text{Ar}/^{39}\text{Ar}$), and are slightly shifted for clarity to prevent overlapping data points. (a) Individual quartz phenocrysts (this study) and bulk quartz analyses (Hildreth *et al.*, 1984). (b) Zircon, sanidine (individual phenocrysts) and obsidian; abraded zircon cores are shown as filled diamonds. (c) Post-LCT intra-caldera lava flows; the ranges of individual quartz grains are shown as boxes. Zircons are plotted by size of analyzed fractions, plus abraded crystal cores and calculated rim compositions. (d) $\Delta^{18}\text{O}(\text{Qz-Zrc})$ for LCT and post-LCT lavas. The equilibrium value of $\Delta^{18}\text{O}(\text{Qz-Zrc})$ is from Fig. 5. (Note that non-equilibrated phenocrysts occur only on low- $\delta^{18}\text{O}$ magmas.)

similar calculated temperatures of 800–900°C (Table 2). Thus, isotopic fractionations and calculated isotopic temperatures are also expected to be similar, despite significant variations in whole-rock $\delta^{18}\text{O}$. Figure 5 plots $\delta^{18}\text{O}(\text{Qz})$ vs $\delta^{18}\text{O}(\text{Zrc})$. Equilibrium quartz–zircon fractionation (Fig. 5, open squares) is determined to be $2.19 \pm 0.07\text{‰}$ (1σ , $n = 20$ samples). This value is between that predicted by empirical ($2.0 \pm 0.2\text{‰}$, Valley *et al.*, 1994) and theoretical (2.57‰ , Zheng, 1993) calibrations at 850°C. Other fractionations for Yellowstone high-silica rhyolites (excluding low- $\delta^{18}\text{O}$ samples) are: $\Delta^{18}\text{O}(\text{Qz-San}) = 0.75 \pm 0.08\text{‰}$ (1σ , $n = 15$ samples); $\Delta^{18}\text{O}(\text{Qz-Obs}) = 0.35 \pm 0.04\text{‰}$ (1σ , $n = 6$ samples); $\Delta^{18}\text{O}(\text{San-Zrc}) = 1.45 \pm 0.11\text{‰}$ (1σ , $n = 15$ samples); and $\Delta^{18}\text{O}(\text{Obs-Zrc}) = 1.76 \pm 0.19\text{‰}$ (1σ , $n = 6$ samples). The predicted quartz–sanidine equilibration temperature (Clayton *et al.*, 1989), based on our measured fractionation, is $850 \pm 60\text{°C}$, which is in excellent agreement with other temperature estimates (see Table 2).

Oxygen isotope zoning in zircon

The disequilibrium relations for zircons and quartz in low- $\delta^{18}\text{O}$ rhyolites (see Figs 4d and 5) suggest that variability or zoning is present among single zircons. Several tests were designed to evaluate this possibility. Zircons were separated by size and large zircons were air abraded. Larger zircons, as well as cores of air-abraded zircons, are 1–3‰ higher in $\delta^{18}\text{O}$ than zircon in equilibrium with obsidian (see Fig. 4b). Smaller zircons are inferred to have grown later, or exchanged oxygen by diffusion more completely because of large surface/volume ratio. Smaller zircons thus represent the same timing as rims of large zircons. This is the first time oxygen isotope zoning in zircon has been demonstrated and it is significant for tracing magma evolution. Future studies will pursue this using ion microprobe analysis for stable isotope ratios as well as U–Pb age. The $\delta^{18}\text{O}$ differences between larger and smaller zircons prompted the search for isotopic differences between cores and rims of zircons.

Zircon air abrasion

Analysis of groups of air-abraded zircon cores from low- $\delta^{18}\text{O}$ rocks closely approach the normal $\delta^{18}\text{O}$ value for zircon in pre-caldera magmas in some cases. Successive air abrasions were made on abundant zircons in the Blue Creek Flow and Middle Biscuit Basin Flow to measure $\delta^{18}\text{O}$ after each step of rim removal. Values of $\delta^{18}\text{O}$ are plotted as a function of average radii of residual zircon cores (Fig. 6). The upper mark of each bracket shows measured $\delta^{18}\text{O}$ of residual cores and the lower mark is the calculated $\delta^{18}\text{O}$ of the rims. The value in per mil on each curve is the bulk $\delta^{18}\text{O}$ for the whole zircon crystal.

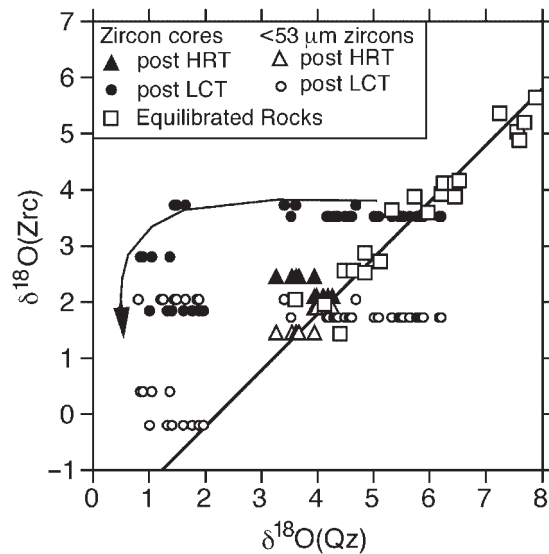


Fig. 5. $\delta^{18}\text{O}(\text{Qz})$ – $\delta^{18}\text{O}(\text{Zrc})$ plot illustrating faster isotopic exchange of individual quartz xenocrysts than zircon. Filled symbols are $\delta^{18}\text{O}$ (Qz, individual phenocrysts)– $\delta^{18}\text{O}$ (Zrc, abraded core) for each sample of low- $\delta^{18}\text{O}$, post-LCT and post-HRT magmas. Open squares are all other lavas that do not show significant quartz and zircon variability. The straight line is the best-fit equilibrium zircon–quartz fractionation of $2.19 \pm 0.07\text{‰}$ (1σ , $n = 20$), corresponding to quartz–zircon equilibrium at 800–900°C (e.g. Zheng, 1993; Valley *et al.*, 1994). Zircon cores in low- $\delta^{18}\text{O}$, post-LCT and post-HRT magmas plot to the left of the line, indicating that quartz exchanged oxygen faster than zircon. The curved arrow is the trajectory of isotopic exchange for one chosen initial $\delta^{18}\text{O}$.

The resulting calculated profile shows an average gradient of $\sim 1\text{‰}$ per 2–3 μm at the rim, and core-to-rim zoning approaches 5‰. Rims are in overall equilibrium with the host glass.

Ion microprobe analyses

The $\delta^{18}\text{O}$ values of the zircon rims were determined by ion microprobe analysis on prismatic crystal faces of zircon grains pressed into indium metal, whereas the $\delta^{18}\text{O}$ of cores of individual crystals were determined in polished grain mounts (Table 4). The average zircon rim $\delta^{18}\text{O}$ is consistent with that predicted from mass balance calculations based on zircon abrasions and for equilibrium with obsidian. Zircons in Lava Creek tuff (sample LCT-3a) do not show $\delta^{18}\text{O}$ zoning. Air abrasion and ion microprobe-measured $\delta^{18}\text{O}$ values of rims in this sample are similar to those of cores, as predicted. In post-LCT and post-HRT lavas, rims of zircon on average are several per mil lower in $\delta^{18}\text{O}$ than cores (samples YL96-4, unit DR, Fig. 1; YL96-20, unit MBB; and BC-1, unit BC, see Fig. 6). Repeated analysis by ion microprobe on the same spot on the face allowed monitoring of $\delta^{18}\text{O}$ vs depth. A typical 20 min analysis penetrated $\sim 2\text{ }\mu\text{m}$ into the crystal after a preliminary $1\text{ }\mu\text{m}$ burn-in, thus making the average depths of the first and second analysis at 2

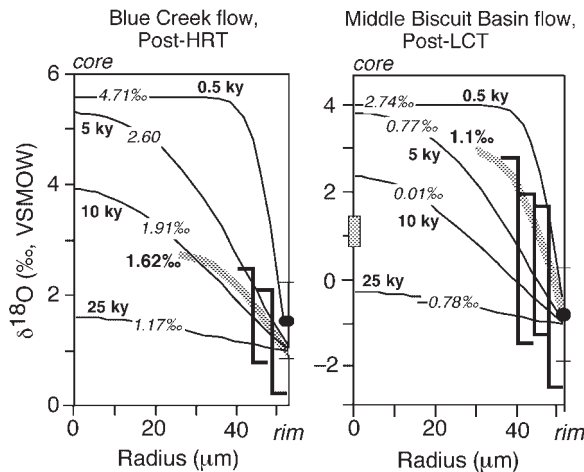


Fig. 6. Zoning profile of $\delta^{18}\text{O}$ in 105 μm diameter (52.5 μm radius) zircons from Blue Creek Flow and Middle Biscuit Basin Flow based on successive air abrasions. The top of each bracket is the average $\delta^{18}\text{O}$ of the residual cores and the bottom of the bracket is the calculated average $\delta^{18}\text{O}$ of material removed for the average radius shown. Thin curves indicate calculated profiles [equation (6.18) of Crank (1975)]. Values in per mil on curves are corresponding $\delta^{18}\text{O}$ of the bulk grain, measured (bold) and calculated (italic) assuming a diffusion profile developed at magmatic temperatures for the time period shown. The steep isotopic gradients and long residence times should be noted. The composition of the rim was calculated based on the measured bulk and the core composition. Compositions of rims, based on analyses of prismatic faces of four individual zircon crystals and determined by the ion microprobe, are shown as filled circle (± 1 SE; see Table 4 for analyses). The measured rim composition is 1–3‰ lighter than the bulk of zircon and the smallest zircons. Stippled bar on the left of MBBF is a measured range of obsidian in the rock; it is in equilibrium with zircon rims.

and 4 μm , respectively. In seven out of nine analyses of zircon faces the second analysis yielded higher $\delta^{18}\text{O}$ with a typical gradient of $\sim 0.5\text{‰}$ per 2 μm (Table 4), consistent with the average gradient predicted from air abrasion (Fig. 6).

The $\delta^{18}\text{O}$ values of zircon cores in two samples (YL96-4 and YL96-2) show large crystal-to-crystal variations. Likewise, rims in YL96-2 (unit SBB) and YL96-18 (unit CF) show larger variability from crystal to crystal, up to the magnitude of core–rim variability (Table 4). Rims on zircons in CF are on average similar to cores and are 5‰ higher in $\delta^{18}\text{O}$ than zircon expected to be in equilibrium with the host rock (Table 3).

The ion microprobe analyses provide the only data for $\delta^{18}\text{O}$ within single zircon crystals, but the spot analyses do not perfectly match the zoning predicted by bulk analyses. Individual zircons represent a mixture of grains of different age and source (Bindeman *et al.*, 2001a), and thus may preserve initial $\delta^{18}\text{O}$ differences between zircon crystals. Although $\delta^{18}\text{O}$ of bulk zircon does not vary significantly in pre-LCT Yellowstone rocks, the range in $\delta^{18}\text{O}$ is from 4 to 6‰. Air abrasion tends to remove the fastest grown pyramids, thus preferentially removing any

overgrowths. Variability of rim compositions may also be related to a sampling bias; the compositions of rims were measured only on the largest crystals (100 $\mu\text{m} \times 200 \mu\text{m}$) and on the slowest-growing prismatic crystal faces.

In contrast to crystal growth, dissolution into melt would act more homogeneously and be less face-selective (e.g. Watson & Harrison, 1983). In particular, if the dissolution of the prismatic faces is faster than the oxygen isotope exchange by diffusion, it will result in retaining relatively higher $\delta^{18}\text{O}$ of the prismatic faces, as seen in some of the ion microprobe analyses. Dissolution and/or reprecipitation, therefore, may compete with diffusive exchange, and are most likely to expose higher- $\delta^{18}\text{O}$ cores on prismatic faces. Additionally, not all zircons float freely in the melt and experience isotropic diffusive exchange with the melt. Many crystals are attached to, or included in, other phenocrysts such as magnetite, quartz and feldspar (see above). The crystal faces of these zircons may not have been in equilibrium with low- $\delta^{18}\text{O}$ melt and each zircon may have experienced different degrees and rates of diffusive exchange with its host melt or phenocrysts. We hypothesize that individual zircon grains may differ in their initial $\delta^{18}\text{O}$, entrapment, overgrowth vs dissolution, and zircon–mineral exchange histories.

Products of major tuff eruptions

Our individual quartz phenocryst $\delta^{18}\text{O}$ analyses in the three major tuff eruptions, Huckleberry Ridge Tuff (HRT, three members: A, B and C), Mesa Falls Tuff (MFT, one member) and Lava Creek Tuff (LCT, two members: A and B), agree well with bulk analyses of quartz phenocrysts from Hildreth *et al.* (1984) (Fig. 4a). Even the $\delta^{18}\text{O}(\text{Qz})$ of the earliest airfall deposits of each eruption is similar to the quartz in bulk magma (Hildreth *et al.*, 1984). Zircon from these voluminous normal- $\delta^{18}\text{O}$ tuffs is in equilibrium with quartz, and the $\delta^{18}\text{O}$ of smaller zircons is similar to $\delta^{18}\text{O}$ of large zircons in the same rock. This implies that these tuffs originated as magmas that were homogeneous and equilibrated with respect to oxygen isotope ratios. The only exception is the Member C of HRT. Despite being more radiogenic in terms of Pb and Sr isotopes (Hildreth *et al.*, 1991), we find that $\delta^{18}\text{O}$ of quartz and zircon in Member C are $\sim 0.5\text{‰}$ higher than for members A and B (Table 3). Member C erupted last in the sequence and is likely to represent deeper layers of an isotopically zoned, batholithic-scale magma chamber, in which there is a subtle downward increase in $\delta^{18}\text{O}$. Values of $\delta^{18}\text{O}$ of individual quartz phenocrysts in members A and B of LCT from different parts of the caldera overlap and are similar to analyses of bulk phenocrysts in Hildreth *et al.* (1984) from 22

Table 4: Ion microprobe analysis of oxygen isotope ratios on the crystal growth faces (Rim) and in polished cores of zircons from rhyolites at Yellowstone

Analysis no.	Sample, crystal-spot	$^{18}\text{O}/^{16}\text{O}$ measured ($\times 1000$)	Internal precision (1 SD $\times 1000$)	$\delta^{18}\text{O}$ VSMOW (‰)	Analysis no.	Sample, crystal-spot	$^{18}\text{O}/^{16}\text{O}$ measured ($\times 1000$)	Internal precision (1 SD $\times 1000$)	$\delta^{18}\text{O}$ VSMOW (‰)
<i>29–31 July 1999</i>									
1	Std-1	1.9400	0.00190	4.6	14	Std-8	1.9412	0.00181	4.7
2	Std-2	1.9392	0.00150	4.2	15	Std-9	1.9451	0.00165	6.7
3	Std-3	1.9371	0.00200	3.2	16	Std-10	1.9407	0.00173	4.5
4	YL96-2, 10-1 CORE	1.9339	0.00203	1.5	17	YL96-2, 8 RIM	1.9360	0.00149	2.1
5	YL96-2, 10-2 CORE R	1.9352	0.00166	2.2	18	YL96-2, 9 RIM R	1.9339	0.00182	1.0
6	YL96-2, 8-1 CORE	1.9335	0.00191	1.3	19	YL96-2, 10 RIM	1.9319	0.00179	0.0
7	YL96-2, 8-2 CORE R	1.9343	0.00165	1.7	20	YL96-2, 11 RIM R	1.9330	0.00204	0.7
8	YL96-2, 7-1 CORE	1.9355	0.00186	2.4	21	YL96-2, 12 RIM R	1.9349	0.00169	1.7
9	YL96-2, 6-1 CORE	1.9347	0.00176	2.0	22	YL96-2, 13 RIM R	1.9369	0.00180	2.7
10	Std-4	1.9395	0.00173	4.5	23	Std-11	1.9387	0.00181	3.7
11	Std-5	1.9432	0.00153	6.4	24	Std-12	1.9411	0.00170	5.0
12	Std-6	1.9419	0.00166	5.7	25	Std-13	1.9425	0.00191	5.7
13	Std-7	1.9433	0.00166	6.4	26	YL96-4, 7 RIM	1.9270	0.00170	-2.3
14	YL96-2, 1 RIM	1.9356	0.00184	2.5	27	YL96-4, 8 RIM R	1.9265	0.00175	-2.5
15	YL96-2, 2 RIM	1.9387	0.00172	4.1	28	YL96-4, 9 RIM	1.9290	0.00174	-1.1
16	YL96-2, 3 RIM	1.9354	0.00172	2.4	29	YL96-4, 10 RIM R	1.9305	0.00165	-0.3
17	YL96-2, 4 RIM	1.9396	0.00174	4.6	30	YL96-4, 11 RIM	1.9306	0.00172	-0.2
18	YL96-2, 5 RIM	1.9351	0.00192	2.3	31	YL96-4, 12 RIM R	1.9316	0.00195	0.3
19	YL96-2, 6 RIM R	1.9361	0.00168	2.8	32	Std-14	1.9411	0.00172	5.3
20	YL96-2, 7 RIM	1.9363	0.00168	2.9	33	Std-15	1.9413	0.00204	5.4
21	Std-8	1.9415	0.00166	5.6	<i>4 August 1999</i>				
22	Std-9	1.9413	0.00180	5.5	10	Std-4	1.9406	0.00170	5.3
23	Std-10	1.9404	0.00201	5.1	11	Std-5	1.9404	0.00174	5.2
24	YL96-4, 1 RIM	1.9293	0.00168	-0.7	12	Std-6	1.9428	0.00193	6.5
25	YL96-4, 2 RIM	1.9283	0.00172	-1.2	13	BC-1, 1 RIM	1.9357	0.00153	2.8
26	YL96-4, 3 RIM	1.9279	0.00168	-1.4	14	BC-1, 2 RIM	1.9330	0.00180	1.4
27	YL96-4, 4 RIM	1.9343	0.00163	1.9	15	BC-1, 3 RIM	1.9296	0.00157	-0.3
28	YL96-4, 5 RIM	1.9307	0.00168	0.1	16	BC-1, 4 RIM	1.9347	0.00196	2.3
29	YL96-4, 6 RIM	1.9272	0.00178	-1.7	17	YL96-20, 1 RIM	1.9278	0.00189	-1.3
30	Std-11	1.9412	0.00186	5.6	18	YL96-20, 2 RIM	1.9294	0.00156	-0.4
31	Std-12	1.9421	0.00158	6.0	19	YL96-20, 3 RIM	1.9305	0.00179	0.2
32	Std-13	1.9405	0.00155	5.2	20	YL96-20, 4 RIM	1.9268	0.00182	-1.8
33	YL96-4, 1-1 CORE	1.9380	0.00164	3.9	21	Std-7	1.9389	0.00184	4.5
34	YL96-4, 4-1 CORE	1.9385	0.00169	4.2	23	Std-8	1.9364	0.00143	3.3
35	YL96-4, 6-1 CORE	1.9295	0.00158	-0.5	24	Std-9	1.9394	0.00178	4.8
36	YL96-4, 6-2 CORE	1.9275	0.00173	-1.5	25	Std-10	1.9379	0.00164	4.0
37	YL96-4, 6-3 CORE	1.9305	0.00187	0.1	26	LCT3A, 1 RIM	1.9388	0.00169	4.5
38	YL96-4, 7-1 CORE	1.9284	0.00163	-1.0	27	LCT3A, 2 RIM	1.9382	0.00161	4.2
39	Std-14	1.9392	0.00192	4.6	28	LCT3A, 3 RIM	1.9379	0.00168	4.0
40	Std-15	1.9439	0.00183	7.0	29	LCT3A, 4 RIM	1.9357	0.00183	2.9
41	Std-16	1.9383	0.00167	4.2	30	YL96-18, 1 RIM	1.9398	0.00157	5.0
42	Std-17	1.9386	0.00186	4.3	31	YL96-18, 2 RIM	1.9354	0.00176	5.0
43	Std-18	1.9385	0.00171	4.3	32	YL96-18, 3 RIM	1.9395	0.00155	4.9
<i>31 July-1 August 1999</i>									
12	Std-6	1.9439	0.00156	6.0	33	YL96-18, 4 RIM	1.9409	0.00150	5.0
13	Std-7	1.9378	0.00172	2.9	34	Std-11	1.9413	0.00182	5.9
					35	Std-12	1.9410	0.00199	5.7
					36	Std-13	1.9401	0.00178	5.0

RIM, analysis of the prismatic crystal growth faces of a euhedral zircon; CORE, analysis of a polished grain mount; R, repeat analysis in the same pit as the preceding analysis (depth profile); Std-*n* represents spot analyses on homogeneous KIM-5 zircon ($\delta^{18}\text{O} = 5.04\text{‰}$). [See text and Valley *et al.* (1998) for analytical details.]

locations, confirming that there are no significant lateral or spatial variations. Furthermore, among individual quartz phenocrysts (14 in LCT, six in MFT and 20 in HRT), we found no low- $\delta^{18}\text{O}$ xenocrysts.

Post-caldera lavas

Post-HRT (first) cycle

Two low- $\delta^{18}\text{O}$ lava flows followed the Huckleberry Ridge Tuff eruption: the Blue Creek Flow and Headquarters Flow. The Blue Creek Flow is similar with respect to trace elements, and in Pb and Sr isotope ratios to member C of HRT (Hildreth *et al.*, 1991), whereas the Headquarters Flow is distinct. We found differences between the two flows in $\delta^{18}\text{O}$ of zircon and quartz. Zircons in the Blue Creek Flow are zoned by at least by 3‰, as revealed by air abrasion and ion microprobe analysis (Fig. 6). Individual quartz phenocrysts also show larger variability (0.7‰) than is typical for equilibrated rocks. The Headquarters Flow, in contrast, contains fully equilibrated quartz, and abraded zircon cores are only 0.18‰ higher in $\delta^{18}\text{O}$ than the bulk (see Table 3). Bishop Mountain Flow, which postdates the low- $\delta^{18}\text{O}$ flows, contains fully equilibrated quartz and zircon with more normal $\delta^{18}\text{O}$ values.

Post-MFT (second) cycle

No significant $\delta^{18}\text{O}$ depletion in or around Henry Forks Caldera has been found after eruption of the Mesa Falls Tuff. Quartz, zircon, sanidine, and obsidian are in overall equilibrium. However, abraded zircon cores in Warm River Butte Flow (WRB), which erupted shortly after MFT, and in Harlequin Flow, erupted later than WRB, are 0.4–0.6‰ higher in $\delta^{18}\text{O}$ (by >2 SD) than the value for bulk zircons or smaller zircons. This suggests a modest core–rim zoning, ~ 1.5 ‰. Post Warm River Butte lavas have nearly constant $\delta^{18}\text{O}$ values for both quartz and zircon, and are similar to those of LCT. Given the distribution of post-MFT rocks around the Yellowstone caldera (Table 1, Fig. 1), it can be assumed that post-MFT lavas (and their plutonic counterparts) form much of the basement and may serve as country (source?) rocks beneath the LCT and rhyolites of the last eruptive cycle.

Post-LCT (third, or last) cycle

A dramatic ^{18}O depletion is seen in lavas and tuffs erupted inside Yellowstone Caldera after the Lava Creek Tuff eruption. Post-LCT lavas erupted outside of the caldera have higher $\delta^{18}\text{O}$ values than LCT (Fig. 4a; also Hildreth *et al.*, 1984). Both quartz and zircon in low- $\delta^{18}\text{O}$ lavas show significant $\delta^{18}\text{O}$ heterogeneity (see Fig. 4c), whereas obsidian and feldspar are homogeneous within analytical precision. Values of $\delta^{18}\text{O}$ in many quartz phenocrysts in

South Biscuit Basin Flow approach +6‰, similar to $\delta^{18}\text{O}$ in quartz from LCT. Cores of abraded zircons from South Biscuit Basin and Canyon Flows are +3.5‰, approaching the pre-caldera value of +4‰. Successive air abrasion of larger zircons ($>105\ \mu\text{m}$) from Middle Biscuit Basin Flow, and ion microprobe analyses of zircon rims (Table 4) allow reconstruction of a zoning profile (Fig. 6). Given the steep gradient of the zoning profile, it is likely that innermost cores (unattainable by abrasion) in MBB (and likewise DR flows) also approach pre-caldera values of +4‰. It is significant that most smaller zircons ($<53\ \mu\text{m}$) have 1‰ higher $\delta^{18}\text{O}$ than the calculated rim composition of larger zircons based on zircon abrasion. This suggests that even the smallest zircons are isotopically zoned, with higher $\delta^{18}\text{O}$ cores and lower $\delta^{18}\text{O}$ rims. In this case, the high- $\delta^{18}\text{O}$ zircon cores suggest that most of the zircons are xenocrysts and that isotopic exchange with low $\delta^{18}\text{O}$ magma shifted the bulk $\delta^{18}\text{O}$ values of smaller zircons more than that of larger zircons because of their higher surface area/volume ratio. The zircon zoning and disequilibria are confined to ^{18}O -depleted intra-caldera rhyolites erupted <150 ky after LCT. This zoning and disequilibria are not seen in rhyolites erupted >150 ky after LCT (Fig. 4d). In particular, the voluminous Scaup Lake, West Yellowstone, and Aster Creek Flows, and the less voluminous North Biscuit Basin Flow, show no significant heterogeneity in $\delta^{18}\text{O}$ of quartz phenocrysts, no $\delta^{18}\text{O}$ zoning in zircon and no quartz–zircon disequilibria.

DISCUSSION

The 2–3‰ variability among individual phenocrysts of quartz in low- $\delta^{18}\text{O}$ lavas has not been observed in other calderas, in part because individual quartz phenocryst analyses are not routinely performed. Quartz phenocrysts in single pumice clasts of the Bishop Tuff, and intra-caldera lavas and voluminous low- $\delta^{18}\text{O}$ tuffs of Timber Mountain–Oasis Valley caldera complex (I. N. Bindeman & J. W. Valley, unpublished data, 2000) do not show such variable values. Analyses of individual quartz phenocrysts are nearly identical to the bulk, and the variability is uniformly low (<0.4 ‰). Thus, the variability of phenocrysts is specific to Yellowstone's low- $\delta^{18}\text{O}$ volcanic rocks and is indicative of their genesis.

We emphasize that because zoned and normal- $\delta^{18}\text{O}$ zircons and quartz phenocrysts occur in homogeneous low- $\delta^{18}\text{O}$ glass, exchange of oxygen is likely, and probably took place through diffusion and solution–reprecipitation. Even if only diffusion is considered, any initial $\delta^{18}\text{O}$ variations in melt disappear several orders of magnitude faster (Zhang *et al.*, 1991) than variations in quartz and zircon (Farver & Yund, 1991; Watson & Cherniak, 1997).

For quartz, solution–reprecipitation is potentially a faster process of exchange than diffusion, as silica (unlike zirconia) is a major constituent of rhyolites. Furthermore, the diffusion of silica in water-bearing rhyolite at 750–850°C is 3×10^{-10} to 9×10^{-11} cm²/s (Baker, 1991). Diffusion of silica in melt is 1–2 orders of magnitude faster than even ‘wet’ diffusion of oxygen in quartz at 750–850°C [1.4×10^{-12} to 1.1×10^{-13} cm²/s, Farver & Yund (1991) and therein]. Solution–reprecipitation features, such as truncation of growth zones by penetrating melt inclusions, are seen in CL images of some quartz phenocrysts (e.g. Fig. 2), but mostly quartz exhibits concentric CL zoning indicative of steady growth. Therefore, diffusive exchange following crystallization appears to be the dominant mechanism of isotope exchange in quartz, although diffusion distances may be significantly reduced by melt inclusions.

For zircon, diffusion may dominate over new growth or solution–reprecipitation. Oxygen diffusion coefficients at $P_{H_2O} > 70$ bars in zircon residing in $\sim 850^\circ\text{C}$ water-bearing magmas are determined experimentally to be of the order of 10^{-17} cm²/s (Watson & Cherniak, 1997). At this diffusion rate, a typical zircon grain of 50 μm radius would exchange and nearly equilibrate after a few tens of thousands of years. The rate of zircon growth in magmas is controlled by sluggish Zr diffusion in melt. Dissolution experiments suggest that it would take as long or longer to crystallize a new 50 μm zircon grain as to exchange it by diffusion. For instance, a zircon of 50 μm radius would grow in 150 ky at a linear growth rate of 10^{-15} cm/s (Watson, 1996). Zircon crystal size distributions (Appendix) would be consistent with 1.56–2.27 $\mu\text{m}/\text{ky}$ growth at this rate. We conclude that both diffusive exchange and new overgrowth played a role in the isotopic exchange of zircon, quartz and magma.

Modeling of diffusive isotope exchange and re-equilibration

The core-to-rim $\delta^{18}\text{O}$ zoning observed in zircons from low- $\delta^{18}\text{O}$ rhyolites (Fig. 6) indicates that zircons (and quartz) with normal $\delta^{18}\text{O}$ values were immersed into low- $\delta^{18}\text{O}$ melt. Such xenocrysts of zircon and quartz will exchange at different rates creating disequilibrium values of $\Delta^{18}\text{O}(\text{Qz-Zrc})$ as shown in Figs 4d, 5 and A2 (Appendix). If given enough time, exchange will become complete and xenocrysts will re-equilibrate at lower $\delta^{18}\text{O}$.

Diffusive exchange of oxygen isotopes in quartz and zircon was modeled [equation (6.18), Crank, 1975] for diffusion in a sphere surrounded by an infinite reservoir (magma) at 750–850°C. Below, we describe results of modeling at 850°C, the near-liquidus conditions for Yellowstone magmas (Table 2); rates of diffusive exchange

at near-solidus temperatures of $\sim 750^\circ\text{C}$ are ~ 10 times slower. Most exchange occurs at higher temperatures and the model below constrains the minimum time necessary for diffusive exchange.

The zoning profiles and the bulk composition of whole zircons (Fig. 6) can be compared with those of the diffusion model. The measured zoning profile of $\delta^{18}\text{O}$ in zircons from Blue Creek Flow (Fig. 6) fits between that predicted for 5–10 ky of residence of normal- $\delta^{18}\text{O}$ zircon (+5.6‰) in low- $\delta^{18}\text{O}$ melt (+2.8‰, in equilibrium with +1.0‰ zircon). Normal (+4‰) zircons in Middle Biscuit Basin Flow would require 500–5000 years to develop the observed zoning.

Figure 7 puts the observed variations in $\delta^{18}\text{O}$ of both quartz and zircon, and $\Delta(\text{Qz-Zrc})$ for lava flows, into a single model of isotopic exchange (Bindeman & Valley, 2000). Crystals of different size were chosen (similar to those observed) and the $\delta^{18}\text{O}$ (core) in each crystal was calculated and compared with the average $\delta^{18}\text{O}$ for the whole crystal. For zircons, we also consider the case in which a new overgrowth forms at a constant rate. The curves of $\delta^{18}\text{O}$ exchange and equilibration result from different rates of diffusive exchange. The key observation in Fig. 7 is that intervals of the maximum $\delta^{18}\text{O}$ zoning within quartz and within zircon do not generally overlap because diffusion in zircon is much slower. The maximum deviations from equilibrium for core or bulk compositions occur at transient times (Fig. 7b). During these times, $\Delta(\text{Qz-Zrc})$ shows wide variations similar to that observed in low- $\delta^{18}\text{O}$ lavas (Fig. 4d). Quartz–zircon disequilibrium, therefore, serves as a gauge for estimating the time of diffusive exchange in magmas.

In Fig. 7a, we also plot the measured range of $\delta^{18}\text{O}$ in zircon, and the observed variability for individual quartz phenocrysts in each unit between the calculated core and bulk curves. Variability of quartz in SBB and CF suggests shorter times of exchange (~ 200 –500 years), which can be inferred from the observation that quartz in these units has the largest variability, whereas slower-exchanging zircon has barely exchanged. DR erupted on top and shortly after CF (Gansecki *et al.*, 1996; Bindeman *et al.*, 2001a). DR may represent the same magma as CF, in which quartz had more time to exchange. Quartz phenocrysts in MBB and DR show only limited remaining heterogeneity, whereas zircons are most zoned (Fig. 4c). This suggests that the time scale for MBB and DR magmas was long enough for quartz equilibration, but not long enough for zircons to fully equilibrate [equivalent to 10^2 – 10^3 years for $\Delta(\text{Qz-Zrc})$ bulk in Fig. 7b]. The diffusion calculations indicate that the time between the beginning of exchange and eruption was of the order of hundreds to thousands of years. For other low- $\delta^{18}\text{O}$ lavas, which show no zoning in zircon and erupted significantly after LCT (e.g. WY, AC, ML),

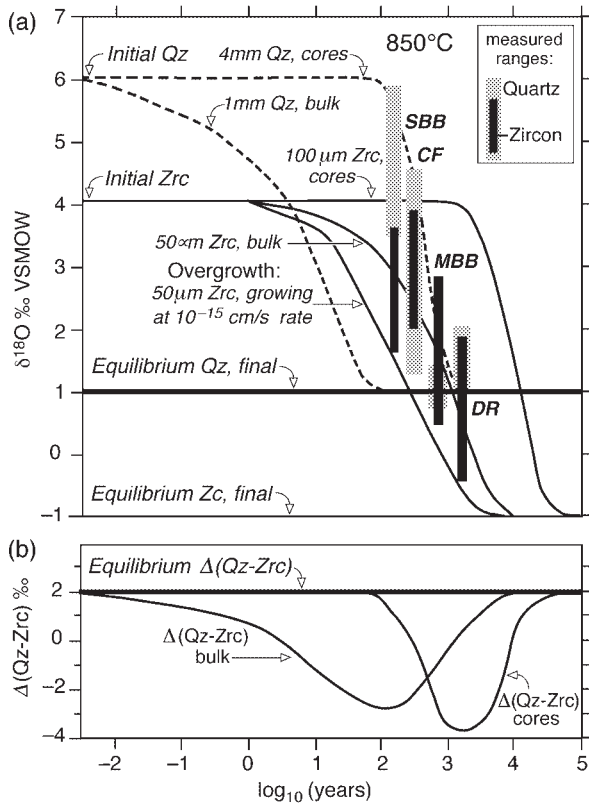


Fig. 7. Diffusive exchange of normal $\delta^{18}\text{O}$ zircon (thick lines) and quartz (dotted lines) xenocrysts with low- $\delta^{18}\text{O}$ melt. 'Wet' diffusion coefficients for oxygen in zircon (Watson & Cherniak, 1997) and quartz (Farver & Yund, 1991) were used. (See text for discussion.) Cores are the innermost 40% of the crystal's radius. Initial quartz and zircon are $+6.0\text{‰}$ and $+4.0\text{‰}$, respectively, corresponding to pre-caldera values; $\delta^{18}\text{O}$ of melt is 0.0‰ , corresponding to a low- $\delta^{18}\text{O}$ magma in equilibrium with quartz of $+1.0\text{‰}$ and zircon of -1.0‰ . A magmatic temperature of 850°C was assumed. Fall in temperature proportionally increases the time of equilibration (~ 10 times per 100°C) without changing the relative position of curves. If solution-precipitation plays an important role in quartz crystallization, then it may anneal internal $\delta^{18}\text{O}$ heterogeneities faster than 'wet' diffusion. Thus, the diffusion calculation for quartz provides an upper time limit for $\delta^{18}\text{O}$ re-equilibration of xenocrysts and melt.

or after HRT (BM), the residence time could have been significantly longer.

Origin of low- $\delta^{18}\text{O}$ magmas of Yellowstone

The equilibration calculations (see Figs 6 and 7) suggest that at least a few hundred years are necessary to develop $\delta^{18}\text{O}$ zoning in quartz and zircon. These calculations also bracket the maximum time limit needed to preserve this heterogeneity, ~ 25 ky. This time interval is an important constraint for any model.

Previous models

The original and attractive model of 'catastrophic' meteoric water-magma interaction during caldera collapse (e.g. Hildreth *et al.*, 1984) is not supported by our data on $\delta^{18}\text{O}$ zoning in zircon and quartz from low- $\delta^{18}\text{O}$ lavas. The length of time required to create zoned xenocrysts is too great. Assimilation (bulk or partial) and magma mixing can create low- $\delta^{18}\text{O}$ magmas (e.g. Taylor, 1986; Bacon *et al.*, 1989; Balsley & Gregory, 1998; Bacon *et al.*, 2000), but we present three arguments against these possibilities.

First, the observed low- $\delta^{18}\text{O}$ magmas of Yellowstone have $\delta^{18}\text{O}$ from 0 to $+3\text{‰}$ and such values are restricted by mass balance. In the extreme case of mixing equal proportions of normal ($+6\text{‰}$) magma and ^{18}O -depleted magma or rock, the $\delta^{18}\text{O}$ (bulk assimilated) would have to be $< -6\text{‰}$ to create magma at 0‰ . Mixing with an ultra-low- $\delta^{18}\text{O}$ magma ($< -5\text{‰}$) is unlikely because no ultra-low- $\delta^{18}\text{O}$ individual phenocrysts of quartz and zircon (Tables 3 and 4) have been found. Furthermore, there is no known source for the genesis of such very low- $\delta^{18}\text{O}$ magmas nor are any wall rocks at Yellowstone observed with sufficiently low $\delta^{18}\text{O}$.

Second, it is difficult to mix tens to hundreds of cubic kilometers of two viscous rhyolite magmas and achieve the textural, chemical and isotopic homogeneity observed in volcanic glass of Yellowstone lavas. The uniformity of $\delta^{18}\text{O}$ (within $\pm 0.5\text{‰}$, Table 3) in individual obsidian spheres in low- $\delta^{18}\text{O}$ rocks is not consistent with the magma mixing model.

Third, in assimilation of low- $\delta^{18}\text{O}$ rocks models, the heat balance controls the maximum amount of assimilation. If all the heat comes from the crystallization of the parent magma, then, of the maximum possible, assimilation is 50% before the magma becomes 100% crystalline, given the similar chemistry (and heat capacities) of both the magma and the assimilate. The observed low- $\delta^{18}\text{O}$ rhyolites are, on the contrary, crystal poor ($< 15\%$), showing that the percentage of any assimilation was small.

The bulk melting-caldera collapse (BMCC) model

We propose that low- $\delta^{18}\text{O}$ magmas originate as a result of the nearly total, bulk melting of hydrothermally altered, low- $\delta^{18}\text{O}$ rocks after caldera collapse. The source rock must be strongly depleted in ^{18}O as is expected in the roof zone of large, shallow magma chambers. Depletion results from circulation of meteoric water, and hydrothermal alteration of volcanic glass and possibly all other phenocrysts, except alteration-resistant quartz and zircon (Criss & Taylor, 1986; Gilliam & Valley, 1997). One example of such alteration is exposed in outcrop: the quartz and zircon in pervasively altered Canyon Flow (sample CF-1, see Tables 1-3) preserve $\delta^{18}\text{O}$ values

similar to those of quartz and zircon in unaltered samples.

We have demonstrated above that quartz and zircons in low- $\delta^{18}\text{O}$ magmas are higher in $\delta^{18}\text{O}$ than would be in equilibrium with their host low- $\delta^{18}\text{O}$ magmas, and zircons contain cores similar to pre-caldera rhyolites. Thus, these zircons did not crystallize from the magma in which they now reside. The most feasible way to disperse zircon xenocrysts in a viscous low- $\delta^{18}\text{O}$ magma would be by near-total fusion of low- $\delta^{18}\text{O}$ source rock(s) containing these zircons. The deficiency of smaller zircons with larger surface to volume ratio (Fig. A1, Appendix) may support the evidence of preferential dissolution of smaller grains, and survival of larger cores in the event of melting. The same argument applies to quartz, which shows lesser abundance, smaller sizes and resorbed morphology in low- $\delta^{18}\text{O}$ lavas.

We propose that remelting of hydrothermally altered roots of down-dropped blocks following caldera collapse creates low- $\delta^{18}\text{O}$ magmas with normal- $\delta^{18}\text{O}$ xenocrysts. Pre-caldera lavas and tuffs are the most likely source rock for remelting. They have less variable $\delta^{18}\text{O}(\text{Qz})$ (5.5–7.5‰) and $\delta^{18}\text{O}(\text{Zrc})$ (3.5–5.5‰) than low- $\delta^{18}\text{O}$ lavas. Trace element similarity of low- $\delta^{18}\text{O}$ rhyolites to normal- $\delta^{18}\text{O}$ pre-caldera rhyolites (e.g. Fig. 3), and not to Archean basement or Eocene Absaroka volcanic rocks, makes them possible intra-caldera substrate for melting.

SHRIMP dating of 89 grains of zircon in LCT, HRT and post-LCT lavas (Bindeman *et al.*, 2001a) demonstrated no pre-Quaternary ages, and few LCT-aged zircons in post-LCT lavas. These results suggest that pre-Quaternary rocks were not involved in melting, and also that LCT magma (or its crystal rinds, e.g. Mahood, 1990) was not a dominant source for post-LCT low- $\delta^{18}\text{O}$ rhyolites. The latter conclusion is also supported by $^{40}\text{Ar}/^{39}\text{Ar}$ individual feldspar age data (Gansecki *et al.*, 1996). Zircon age spectra in each post-LCT low- $\delta^{18}\text{O}$ lava (CF, DR, MBB) consist of three distinct age groups: 2.1 ± 0.4 Ma (consistent with HRT), $1.0\text{--}0.7$ Ma (pre-LCT volcanic rocks) and the eruption age of $0.5\text{--}0.6$ Ma. These age spectra in each low- $\delta^{18}\text{O}$ lava suggest that post-LCT low- $\delta^{18}\text{O}$ melts originated from more than one source rock, notably HRT and pre-LCT volcanic rocks, residing in the down-dropped intra-caldera block.

Caldera collapse and low- $\delta^{18}\text{O}$ rhyolites

We consider caldera collapse as essential for formation of low- $\delta^{18}\text{O}$ rhyolites at Yellowstone. The absence of low- $\delta^{18}\text{O}$ xenocrysts in HRT and LCT argues against the existence of a significant low- $\delta^{18}\text{O}$ magma layer(s) in any of the dominant magma chambers, which could result from the melting of low- $\delta^{18}\text{O}$ roof rock before caldera formation.

Figure 8 illustrates the main points of the bulk melting–caldera collapse (BMCC) model. Before caldera collapse,

intensive hydrothermal alteration by heated surface waters lowers the $\delta^{18}\text{O}$ of country rocks (Stage I). The roof of the magma chamber (source rocks to low- $\delta^{18}\text{O}$ rhyolites) becomes low in $\delta^{18}\text{O}(\text{WR})$ through alteration of feldspars and glass, but not quartz and zircon. Studies of $\delta^{18}\text{O}$ in whole rocks, glass and quartz in drill holes of ~ 2 km depth in Bishop tuff within Long Valley caldera show that quartz survives hydrothermal alteration, and that the degree of whole-rock ^{18}O depletion increases with depth and temperature (Smith & Suemnicht, 1991; McConnell *et al.*, 1997). Similar results were obtained at Yellowstone (Sturchio *et al.*, 1990).

Caldera collapse (Stage II, Fig. 8) brings the base of the hydrothermally altered, low- $\delta^{18}\text{O}(\text{WR})$ down-dropped block closer to the hot interior of the magma chamber. The failure of non-rhyolitic magma to erupt during major caldera-forming events suggests that most magma was not erupted and remained in batholith-scale magma chambers, parental to LCT and HRT (e.g. Smith, 1979). The conservative estimate of vertical drop as a result of caldera subsidence after the eruption of 1000 km^3 of LCT is 500 m based on an eruptive volume–caldera area argument (Smith, 1979; Hildreth *et al.*, 1984). R. L. Christiansen (personal communication, 2001) estimates the minimum down-drop of 600 m after LCT, and 700 m after HRT, based on the projection of thickness of LCT and HRT from caldera walls. It is also possible that the vertical drop is a few times larger. For example, the Long Valley caldera comparable in size with Yellowstone caldera formed by eruption of 650 km^3 of Bishop Tuff, and subsided 2–3 km, as demonstrated by the thickness of intra-caldera tuff (McConnell *et al.*, 1995). The vertical drop could be even larger following eruption of 2500 km^3 of HRT (Smith & Christiansen, 1980), but still smaller than the vertical dimension of most batholiths (of 5–15 km; Ague & Brandon, 1996; Anderson *et al.*, 1997).

It is possible that caldera collapse caused fresh basalt to underplate the floor of the magma chamber soon after climatic eruption, as the denser basalt would compensate for the isostatic deficiency after removal of up to thousands of cubic kilometers of rhyolite. Basalt would also provide heat for subsequent melting of low- $\delta^{18}\text{O}$ rocks. However, no basalt erupted with, or immediately after, eruption of low- $\delta^{18}\text{O}$ magmas. If basalt underplating occurred, the layer of remaining LCT magma between the down-dropped block and the underplating magma appears to have served as a density filter.

In Stage III (Fig. 8), remelting of the roots of the down-dropped block forms pockets of low- $\delta^{18}\text{O}$ magma near the roof of the magma chamber. As most Yellowstone rhyolites are high-silica, near-cotectic melts, crystallization modeling (MELTS; Ghiorso & Sack, 1995) above shows that a temperature rise of from 710°C to over $800\text{--}850^\circ\text{C}$ yields $\sim 100\%$ melting. The melting could have proceeded at lower temperatures than the

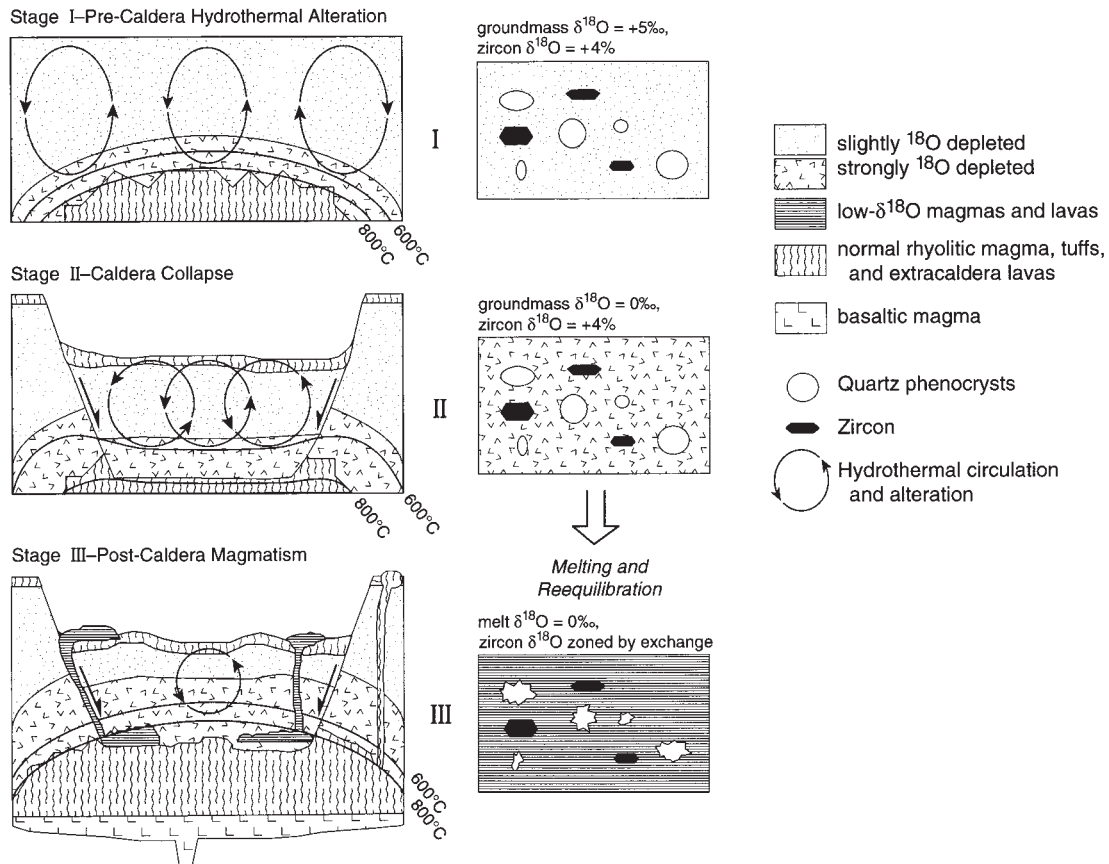


Fig. 8. The bulk melting–caldera collapse model for genesis of low- $\delta^{18}\text{O}$ magma. Stage I: hydrothermal alteration creates low- $\delta^{18}\text{O}$ country rocks adjacent to the magma chamber; more alteration occurs nearest magma at higher temperatures. Quartz and zircons are not altered by hydrothermal fluids and retain their pre-caldera $\delta^{18}\text{O}$ values. Stage II: caldera collapse brings low- $\delta^{18}\text{O}$ rocks with unaltered quartz and zircon into the magma chamber. This promotes nearly complete and rapid melting in which zircon and some quartz survive unexchanged as normal- $\delta^{18}\text{O}$ xenocrysts in newly formed low- $\delta^{18}\text{O}$ magma pockets. Quartz and zircon xenocrysts are variably exchanged with low- $\delta^{18}\text{O}$ melt before eruption and the amount of exchange reflects the longevity of the magma. Stage III: low- $\delta^{18}\text{O}$ magmas erupt in different parts of the caldera.

temperature in the interior of the magma chamber, possibly facilitated by the water-richer nature of hydrothermally altered source rocks. The pockets of newly formed rhyolitic melt may have been near, but not necessarily at, the contact with the main magma chamber itself. There could have been screens between low- $\delta^{18}\text{O}$ magma and the main chamber composed of (1) pre-existing or newly formed crystal rinds of the magma chamber, and/or (2) older (pre-Quaternary) rocks with higher melting temperature. Pre-Quaternary rocks probably participated in exchange with magma following HRT eruption, as HRT member C and post-HRT Blue Creek low- $\delta^{18}\text{O}$ lava flow are more radiogenic (Hildreth *et al.*, 1991). However, by the LCT cycle, either pre-Quaternary rocks in the intra-caldera block were completely digested or lower-temperature melting components were exhausted.

The most ^{18}O -depleted source rocks were originally concentrated close to the magma chamber, where Stage

I hydrothermal alteration was most intense. They thus melted first, giving rise to low- $\delta^{18}\text{O}$ magmas, which erupted independently near the eastern and western resurgent domes (ML and SCRD in Fig. 1) of the last Yellowstone caldera, preserving local chemical (e.g. Fig. 3, Table 2) and $\delta^{18}\text{O}$ variability of the parent source. The coeval relations between post-caldera resurgence and the appearance of low- $\delta^{18}\text{O}$ lavas may serve as geological evidence of the melting in the down-dropped block, which caused local isostatic rebound. Each lava formed by this process and was homogenized within itself, but contained xenocrystic quartz and zircon inherited from the source (Fig. 8, Stage III). We favor the formation of isolated ‘pockets’ of melt, rather than a well-mixed layer of low- $\delta^{18}\text{O}$ magma on the top of the magma chamber. As post-collapse, low- $\delta^{18}\text{O}$ magmas are chemically similar to pre-caldera normal- $\delta^{18}\text{O}$ lavas, they must have been derived from remelting of chemically similar, but ^{18}O -depleted (hydrothermally altered)

rhyolites, products of previous magmatic activity. This explains why the first magmas to appear after LCT (CF, MBB, DR), and after HRT (BC, HQ) caldera collapses are the most ^{18}O depleted. The isotopic 'recovery' toward the less ^{18}O -depleted compositions of younger intra-caldera lavas could result from mixing with normal magma from the interior, as was suggested previously (e.g. Hildreth *et al.*, 1984, 1991). We suggest that this recovery is more probably the result of progressive remelting of less ^{18}O -depleted rocks of the caldera block farther from the magma chamber.

Other calderas and the origin of intra-caldera volcanism

The BMCC model is not restricted to the genesis of low- $\delta^{18}\text{O}$ magmas. This process of shallow remelting is likely to be widespread and may characterize many other calderas that do not have recognizable ^{18}O depletions. Total remelting of geochemically similar rhyolites of pre-caldera rocks using only heat but not matter from the dominant magma is an important newly proposed process of intra-caldera volcanism. It is largely cryptic and can best be discovered using oxygen isotope analyses, but it may be important in calderas where distinctive, low- $\delta^{18}\text{O}$ magmas do not occur. The BMCC model is significantly different from older models in which the dominant magma assimilates roof rocks. The BMCC model is helpful for explaining post-caldera volcanism and resurgence, and assessing chemical evolution, and the energy balance that is pertinent to volcanic hazards.

ACKNOWLEDGEMENTS

We are grateful to Mike Spicuzza (Madison) and John Craven (Edinburgh) for support during isotope analyses; John Fournelle for help with SEM and CL imaging of quartz and electron microprobe analysis of zircons; Carrie Gilliam, Curtis Manley and Lena Bogolubova for help with sample collection; Kristin Greene for help with zircon separation; and Brian Hess for polishing thin sections and grain mounts. Mike Spicuzza, Liz King and Jade Star Lackey provided informal comments on the manuscript. William Peck helped with ion microprobe analyses. Reviews by Wes Hildreth, William Nash and Steve Balsley, and editorial suggestions of George Bergantz are gratefully acknowledged. This research was supported by the DOE (grant FGO2-93ER14389) and NSF (grant EAR96-28142).

REFERENCES

- Ague, J. J. & Brandon, M. T. (1996). Regional tilt of the Mount Stuart Batholith, Washington, determined using aluminum-in-hornblende

barometry; implications for northward translation of Baja British Columbia. *Geological Society of America Bulletin* **108**, 471–488.

- Anderson, A. T., Davis, A. M. & Lu, F. (2000). Evolution of Bishop Tuff rhyolitic magma based on melt and magnetite inclusions and zoned phenocrysts. *Journal of Petrology* **41**, 440–473.
- Anderson, J. L., Ague, J. J. & Brandon, M. T. (1997). Regional tilt of the Mount Stuart Batholith, Washington, determined using aluminum-in-hornblende barometry; implications for northward translation of Baja British Columbia; discussion and reply. *Geological Society of America Bulletin* **109**, 1223–1227.
- Bacon, C. R., Adami, L. H. & Lanphere, M. A. (1989). Direct evidence for the origin of low- $\delta^{18}\text{O}$ silicic magmas: quenched samples of a magma chamber's partially-fused granitoid walls, Crater Lake, Oregon. *Earth and Planetary Science Letters* **96**, 199–208.
- Bacon, C. R., Persing, H. M., Wooden, J. L. & Ireland, T. R. (2000). Late Pleistocene granodiorite beneath Crater Lake caldera, Oregon, dated by ion microprobe. *Geology* **28**, 467–470.
- Baker, D. R. (1991). Interdiffusion of hydrous dacitic and rhyolitic melts and the efficacy of rhyolite contamination of dacitic enclaves. *Contributions to Mineralogy and Petrology* **106**, 462–473.
- Balsley, S. D. & Gregory, R. T. (1998). Low- $\delta^{18}\text{O}$ magmas: why are they so rare? *Earth and Planetary Science Letters* **162**, 123–136.
- Bindeman, I. N. & Valley, J. W. (2000). The formation of low- $\delta^{18}\text{O}$ rhyolites after caldera collapse at Yellowstone, Wyoming, USA. *Geology* **28**, 719–722.
- Bindeman, I. N., Valley, J. W., Wooden, J. L. & Persing, H. M. (2001a). Post-caldera volcanism: *in situ* measurement of U–Pb age and oxygen isotope ratio in Pleistocene zircons from Yellowstone caldera. *Earth and Planetary Science Letters* (in press).
- Bindeman, I. N., Fournelle, J. H. & Valley, J. W. (2001b). Low- $\delta^{18}\text{O}$ tephra from a compositionally zoned magma body: Fisher caldera, Unimak Island, Aleutians. *Journal of Volcanology and Geothermal Research* (in press).
- Cashman, K. V. & Ferry, J. M. (1988). Crystal size distribution (CSD) in rocks and the kinetics and dynamics of crystallization. *Contributions to Mineralogy and Petrology* **99**, 401–415.
- Cashman, K. V. & Marsh, B. D. (1988). Crystal size distribution (CSD) in rocks and the kinetics and dynamics of crystallization—II. Makaopuhi lava lake. *Contributions to Mineralogy and Petrology* **99**, 292–314.
- Cherniak, D. J., Hanchar, J. M. & Watson, E. B. (1997a). Rare-earth diffusion in zircon. *Chemical Geology* **134**, 289–301.
- Cherniak, D. J., Hanchar, J. M. & Watson, E. B. (1997b). Diffusion of tetravalent cations in zircon. *Contributions to Mineralogy and Petrology* **127**, 383–390.
- Christiansen, R. L. (1982). Late Cenozoic volcanism of the Island Park area, eastern Idaho. In: Bonnicksen, B. & Breckenridge, R. M. (eds) *Cenozoic Geology of Idaho*. Idaho Bureau of Mines and Geology, Bulletin **26**, 345–368.
- Christiansen, R. L. (1989). The Yellowstone Plateau volcanic field. In: *Field Excursions to Volcanic Terranes in the Western United States, Volume II: Cascades and Intermountain West*. New Mexico Bureau of Mines and Mineral Resources, Memoir **47**, 137–153.
- Christiansen, R. L. & Blank, H. R., Jr (1972a). Volcanic stratigraphy of the Quaternary rhyolite plateau in Yellowstone National Park. *US Geological Survey, Professional Papers* **729-B**, 18 pp.
- Christiansen, R. L. & Blank, H. R., Jr (1972b). *Geologic Map of Yellowstone National Park, WY, Map I-711*. Reston, VA: US Geological Survey.
- Christiansen, R. L. & Blank, H. R., Jr (1974). *Geologic Map of the Madison Junction Quadrangle, Yellowstone National Park, Wyoming, Map GQ-1190*. Reston, VA: US Geological Survey.
- Clayton, R. N., Goldsmith, J. R. & Mayeda, T. K. (1989). Oxygen isotope fractionation in quartz, albite, anorthite and calcite. *Geochimica et Cosmochimica Acta* **53**, 725–733.

- Crank, J. (1975). *The Mathematics of Diffusion*, 2nd edn. Oxford: Oxford University Press.
- Criss, R. E. & Taylor, H. P., Jr (1986). Meteoric–hydrothermal systems. In: Valley, J. W., Taylor, H. P., Jr & O'Neil, J. R. (eds) *Stable Isotopes in High Temperature Geological Processes*. Mineralogical Society of America, *Reviews in Mineralogy* **16**, 373–422.
- Doe, B. R., Leeman, W. P., Christiansen, R. L. & Hedge, C. E. (1982). Lead and strontium isotopes and related trace elements as genetic tracers in the Upper Cenozoic rhyolite–basalt association of the Yellowstone plateau volcanic field. *Journal of Geophysical Research* **87**, 4785–4806.
- Donaldson, C. H. & Henderson, C. M. B. (1988). A new interpretation of round embayments in quartz crystals. *Mineralogical Magazine* **52**, 27–33.
- Farver, J. R. & Yund, R. A. (1991). Oxygen diffusion in quartz: dependence on temperature and water fugacity. *Chemical Geology* **90**, 55–70.
- Fournelle, J. H., Bindeman, I. N., Donovan, J. D. & Valley, J. W. (2000). Quantitative EMPA mapping of zircons from Yellowstone. *EOS Transactions, American Geophysical Union, Spring Meeting* **81**, 26–27.
- Fournier, R. O. (1989). Geochemistry and dynamics of the Yellowstone National Park hydrothermal system. *Annual Review of Earth and Planetary Sciences* **16**, 13–51.
- Friedman, I., Lipman, P. W., Obradovich, J. D., Gleason, J. D. & Christiansen, R. L. (1974). Meteoric water in magmas. *Science* **184**, 1069–1072.
- Gansecki, C. A., Mahood, G. A. & McWilliams, M. O. (1996). $^{40}\text{Ar}/^{39}\text{Ar}$ geochronology of rhyolites erupted following collapse of the Yellowstone caldera, Yellowstone Plateau volcanic field: implications for crustal contamination. *Earth and Planetary Science Letters* **142**, 91–107.
- Gansecki, C. A., Mahood, G. A. & McWilliams, M. O. (1998). New ages for the climactic eruption at Yellowstone: single-crystal $^{40}\text{Ar}/^{39}\text{Ar}$ dating identifies contamination. *Geology* **26**, 343–346.
- Ghiorso, M. S. & Sack, R. O. (1995). Chemical mass-transfer in magmatic processes IV. A revised and internally consistent thermodynamic model for the interpolation and extrapolation of liquid–solid equilibria in magmatic systems at elevated temperatures and pressure. *Contributions to Mineralogy and Petrology* **119**, 197–212.
- Gilliam, C. & Valley, J. W. (1997). Low- $\delta^{18}\text{O}$ magma, Isle of Skye, Scotland: evidence from zircons. *Geochimica et Cosmochimica Acta* **61**, 4975–4981.
- Heaman, L. M. & LeCheminant, A. N. (1993). Paragenesis and U–Pb systematics of baddeleyite (ZrO_2). *Chemical Geology* **110**, 95–126.
- Hildreth, W., Christiansen, R. L. & O'Neil, J. R. (1984). Catastrophic isotopic modification of rhyolitic magma at times of caldera subsidence, Yellowstone Plateau Volcanic Field. *Journal of Geophysical Research* **89**, 8339–8369.
- Hildreth, W., Halliday, A. N. & Christiansen, R. L. (1991). Isotopic and chemical evidence concerning the genesis and contamination of basaltic and rhyolitic magmas beneath the Yellowstone Plateau Volcanic Field. *Journal of Petrology* **32**, 63–138.
- Hinton, R. W. & Upton, B. G. J. (1991). The chemistry of zircon—variations within and between large crystals from syenite and alkali basalt xenoliths. *Geochimica et Cosmochimica Acta* **55**, 3287–3302.
- Hoskin, P. W. O. & Ireland, T. R. (2000). Rare earth element chemistry of zircon and its use as a provenance indicator. *Geology* **28**, 627–630.
- King, E. M., Barrie, C. T. & Valley, J. W. (1997). Hydrothermal alteration of oxygen isotope ratio in quartz phenocrysts, Kidd Creek, Ontario. *Geology* **25**, 1079–1082.
- Larsen, L. H. & Poldervaart, A. (1957). Measurements and distribution of zircons in some granitic rocks of magmatic origin. *Mineralogical Magazine* **31**, 544–564.
- Larson, P. B. & Taylor, H. P., Jr (1986). $^{18}\text{O}/^{16}\text{O}$ ratios in ash-flow tuffs and lavas erupted from the central Nevada caldera complex and the San Juan caldera complex, Colorado. *Contributions to Mineralogy and Petrology* **92**, 146–156.
- Lewis, A. J., Palmer, M. R., Sturchio, N. C. & Kemp, A. J. (1997). The rare earth element geochemistry of acid–sulphate–chloride geothermal systems from Yellowstone National Park, WY, USA. *Geochimica et Cosmochimica Acta* **61**, 695–706.
- Lipman, P. W. & Friedman, I. (1975). Interaction of meteoric water with magma: an oxygen isotope study of ash-flow sheets from southern Nevada. *Geological Society of America Bulletin* **86**, 695–702.
- Mahood, G. A. (1990). Second reply to the Comments of R. S. J. Sparks, H. E. Huppert, and C. J. N. Wilson on 'Evidence for long-residence times of rhyolitic magma in the Long Valley magmatic system: The isotopic record in pre-caldera lavas of Glass Mountain.' *Earth and Planetary Science Letters* **99**, 395–399.
- Marshall, D. J. (1988). *Cathodoluminescence of Geological Materials*. Boston, MA: Unwin Hyman.
- McConnell, V. S., Shearer, C. K., Eichelberger, J. C., Keskinen, M. J., Layer, P. W. & Papike, J. J. (1995). Rhyolite intrusions in the intracaldera Bishop Tuff, Long Valley Caldera, California. *Journal of Volcanology and Geothermal Research* **67**, 41–60.
- McConnell, V. S., Valley, J. W. & Eichelberger, J. C. (1997). Oxygen isotope compositions of intracaldera rocks: hydrothermal history of the Long Valley Caldera, California. *Journal of Volcanology and Geothermal Research* **76**, 83–109.
- Monani, S. & Valley, J. W. (2001). Oxygen isotope ratios of zircon: magma genesis of low- $\delta^{18}\text{O}$ granites from the British Tertiary Igneous Province, western Scotland. *Earth and Planetary Science Letters* **150**, 27–39.
- Muehlenbachs, K., Anderson, A. T. & Sigvaldsson, G. E. (1974). Low- $\delta^{18}\text{O}$ basalts from Iceland. *Geochimica et Cosmochimica Acta* **38**, 577–588.
- Obradovich, J. D. (1992). Geochronology of the Late Cenozoic volcanism of Yellowstone National Park and adjoining areas, Wyoming and Idaho. *US Geological Survey Open-File Report* **92-408**, 1–45.
- Peck, W. H., Valley, J. W. & McLelland, J. (1999). Slow oxygen diffusion in zircon during cooling of Adirondack orthogneiss. *Geological Society of America, Abstracts with Program* **31**, 103.
- Reid, M. R., Coath, C. D., Harrison, M. T. & McKeegan, K. D. (1997). Prolonged residence times for the youngest rhyolites associated with Long Valley Caldera: ^{230}Th – ^{238}U ion microprobe dating of young zircons. *Earth and Planetary Science Letters* **150**, 27–39.
- Rumble, D. & Sharp, Z. D. (1998). Laser microanalysis of silicates for $^{18}\text{O}/^{17}\text{O}/^{16}\text{O}$ and of carbonates for $^{18}\text{O}/^{16}\text{O}$ and $^{13}\text{C}/^{12}\text{C}$ ratios. In: McKibben, M. A., Shanks, W. C. III & Ridley, W. I. (eds) Applications of microanalytical techniques to understanding mineralizing processes. *Society of Economic Geology, Reviews in Economic Geology*, **7**, 99–119.
- Smith, B. M. & Suemnicht, G. A. (1991). Oxygen isotope evidence for past and present hydrothermal regimes of Long Valley caldera, California. *Journal of Volcanology and Geothermal Research* **48**, 319–339.
- Smith, R. L. (1979). Ash-flow magmatism. *Geological Society of America, Special Papers* **180**, 5–27.
- Smith, R. L. & Christiansen, R. L. (1980). Yellowstone Park as a window on the Earth's interior. *Scientific American* **242**(N1), 104–116.
- Spicuzza, M. J., Valley, J. W., Kohn, M. J., Girard, J. P. & Fouillac, A. M. (1998a). The rapid heating, defocused beam technique: a CO_2 -laser-based method for highly precise and accurate determination of $\delta^{18}\text{O}$ values of quartz. *Chemical Geology* **144**, 195–203.
- Spicuzza, M. J., Valley, J. W. & McConnell, V. S. (1998b). Oxygen isotope analysis of whole rocks via laser fluorination: an airlock approach. *Geological Society of America, Abstracts with Program* **30**, 80.

- Sturchio, N. C., Muehlenbachs, K. & Seitz, M. G. (1986). Element redistribution during hydrothermal alteration of rhyolite in an active geothermal system: Yellowstone drill cores Y-7 and Y-8. *Geochimica et Cosmochimica Acta* **50**, 1619–1631.
- Sturchio, N. C., Keith, T. E. C. & Muehlenbachs, K. (1990). Oxygen and carbon isotope ratios of hydrothermal minerals from Yellowstone drill cores. *Journal of Volcanology and Geothermal Research* **40**, 23–37.
- Taylor, H. P., Jr (1986). Igneous rocks: II. Isotopic case studies of circum-pacific magmatism. In: Valley, J. W., Taylor, H. P., Jr & O'Neil, J. R. (eds) *Stable Isotopes in High Temperature Geological Processes. Mineralogical Society of America, Reviews in Mineralogy* **16**, 273–316.
- Taylor, H. P., Jr & Sheppard, S. M. F. (1986). Igneous rocks: I. Processes of isotopic fractionation and isotopic systematics. In: Valley, J. W., Taylor, H. P., Jr & O'Neil, J. R. (eds) *Stable Isotopes in High Temperature Geological Processes. Mineralogical Society of America, Reviews in Mineralogy* **16**, 227–272.
- Terakado, Y. & Fujitani, T. (1998). Behavior of the rare earth elements and other trace elements during interaction between acidic hydrothermal solutions and silicic volcanic rocks, southwestern Japan. *Geochimica et Cosmochimica Acta* **62**, 1903–1917.
- Valley, J. W. & Graham, C. M. (1996). Ion microprobe analysis of oxygen isotope ratios in quartz from Skye granite: healed microcracks, fluid flow, and hydrothermal exchange. *Contributions to Mineralogy and Petrology* **124**, 225–234.
- Valley, J. W., Chiarenzelli, J. R. & McLelland, J. M. (1994). Oxygen isotope geochemistry of zircon. *Earth and Planetary Science Letters* **126**, 187–206.
- Valley, J. W., Kitchen, N., Kohn, M. J., Niendorf, C. R. & Spicuzza, M. J. (1995). UWG-2, a garnet standard for oxygen isotope ratio: strategies for high precision and accuracy with laser heating. *Geochimica et Cosmochimica Acta* **59**, 5223–5231.
- Valley, J. W., Graham, C. M., Harte, B., Kinny, P. & Eiler, J. M. (1998a). Ion microprobe analysis of oxygen, carbon, and hydrogen isotope ratios. In: McKibben, M. A., Shanks, W. C. III & Ridley, W. I. (eds) *Applications of Microanalytical Techniques to Understanding Mineralizing Processes. Society of Economic Geology, Reviews in Economic Geology* **7**, 73–98.
- Valley, J. W., Kinny, P., Schulze, D. J. & Spicuzza, M. J. (1998b). Zircon megacrysts from kimberlite: oxygen isotope variability among mantle melts. *Contributions to Mineralogy and Petrology* **133**, 1–11.
- Vavra, G. (1994). Systematics of internal zircon morphology in major Variscan granitoid types. *Contributions to Mineralogy and Petrology* **117**, 331–344.
- Watson, E. B. (1996). Dissolution, growth and survival of zircons during crustal fusion: kinetic principles, geologic models and implications for isotopic inheritance. *Transactions of the Royal Society of Edinburgh* **87**, 43–56.
- Watson, E. B. & Cherniak, D. J. (1997). Oxygen diffusion in zircon. *Earth and Planetary Science Letters* **148**, 527–544.
- Watson, E. B. & Harrison, T. M. (1983). Zircon saturation revisited: temperature and compositional effects in a variety of crustal magma types. *Earth and Planetary Science Letters* **64**, 295–304.
- Whitney, J. A. (1988). The origin of granite: the role and source of water in the evolution of granitic magmas. *Geological Society of America Bulletin* **100**, 1886–1897.
- Zhang, Y., Stolper, E. M. & Wasserburg, G. J. (1991). Diffusion of water in rhyolitic glasses. *Geochimica et Cosmochimica Acta* **55**, 441–456.
- Zheng, Y. F. (1993). Calculation of oxygen isotope fractionation in anhydrous silicate minerals. *Geochimica et Cosmochimica Acta* **57**, 1079–1091.

APPENDIX: ZIRCON IN YELLOWSTONE MAGMAS

Zirconium distribution

To determine how much of the total whole-rock Zr resides in zircon, 657 g of a glassy rhyolite (sample YL96-4, unit DR, 393 ppm of Zr, Table 2) was digested in HF, and yielded 93 mg of zircon. This corresponds to 141.5 ppm of zircon in the rock, or 70.5 ppm of Zr. Therefore, only 18% of the total zirconium in this sample resides in zircon, whereas most Zr remains in the glass.

Crystal size distribution and shape

Zircon morphology and crystal size distribution (CSD) were used to estimate the residence time of zircon populations at nominal growth rates (Fig. A1). The CSD was measured on bulk zircon separates using digital images and the Scion-NIH image program. The advantage of using individual whole grains for size measurements (as opposed to two-dimensional thin-section images) could be compromised if there was selective loss of smaller grains during zircon separation procedures. To confirm that conventional separation procedures did not bias the original size distribution, the CSD of HF-extracted zircons was compared with that for conventionally extracted zircons (sample YL96-4, unit DR). HF-extracted zircon size distribution overlapped that obtained using the conventional technique (Fig. A1), thus showing no introduced bias.

Most zircons are 30–350 μm long, but rocks with smaller quantities of zircons are characterized by smaller zircons. The majority of zircons, regardless of size, are euhedral tetragonal dipyramids. The average length-to-breadth ratio (L/B) for zircon increases linearly from 1.5:1 for 50 μm length, to 3:1 for zircons of 250 μm length; few zircons have L/B as high as 20. No statistical difference was observed between the rate of L/B increase with L between different rocks, nor was any correlation found as a function of the amount of extracted zircons, rock crystallinity or $\delta^{18}\text{O}$. Similar L/B increase with length was cited to be an intrinsic property of igneous zircons worldwide (e.g. Larsen & Poldervaart, 1957) and is due to faster growth of pyramids vs prismatic faces (Vavra, 1994).

The results of CSD measurements are plotted as the natural log of linear population density vs average crystal length (Fig. A1) with 10 μm sample bins. For each sample, typically >350 zircons were measured. According to CSD theory, slopes taken from Fig. A1 are proportional to $-1/G\tau$, where G is a linear growth rate, and τ is the residence time (Cashman & Marsh, 1988). Assuming a constant growth rate G , this relationship can be used to determine the population residence time τ . Zircon growth

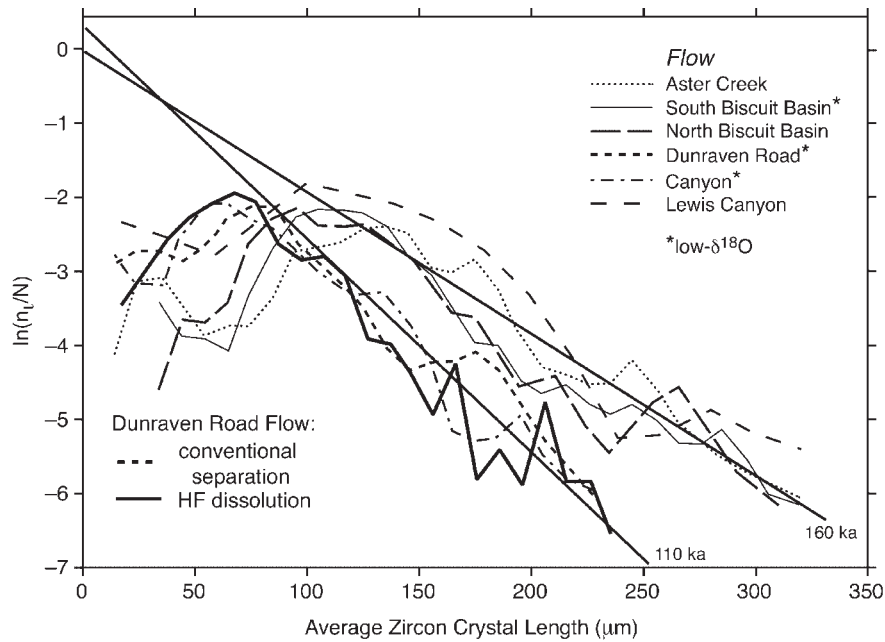


Fig. A1. Zircon crystal size distribution, expressed as the logarithm of population density (n_i/N) vs average crystal length in six lava flows; n_i is the number of crystals of length L (sample bin is $10\ \mu\text{m}$), in a total population N . Each curve is based on measurements of 330–430 crystals; 110 ky and 160 ky are residence times (τ) of zircon populations calculated for $10^{-15}\ \text{cm/s}$ growth rate, G (Watson, 1996), and the equation $d[\ln(n_i/N)]/d(\text{av. length}) = -1/G\tau$ (Cashman & Marsh, 1988). If the growth rates are an order of magnitude faster, the corresponding residence time becomes proportionally shorter.

rates are likely to be limited by diffusion of zirconium in the melt to the growing crystal (Watson & Harrison, 1983; Watson, 1996). Zircon dissolution experiments suggest growth rates on the order of 10^{-15} – $10^{-17}\ \text{cm/s}$ for silicic rocks (Watson, 1996). Given a rate of $10^{-15}\ \text{cm/s}$ and the range of slopes in Fig. A1, the residence time of zircon populations is of the order of 100–200 ky. Zircon residence times determined elsewhere using U–Th disequilibria also are found to be $>100\ \text{ky}$ (Reid *et al.*, 1997). Zircon CSD in lavas erupted in adjacent localities without a significant time gap are remarkably similar. In particular, Dunraven Road Flow erupted after Canyon Flow (as evidenced by field relations and $^{40}\text{Ar}/^{39}\text{Ar}$ age, Table 1). These two flows have similar size distribution and estimated residence time, which suggests that no new zircon growth occurred in the magma chamber between the CF and DR eruptions. Progressively decaying nucleation rates, Ostwald ripening or ‘annealing’ (Cashman & Ferry, 1988) leads to the preferential growth of large zircon grains at the expense of small ones and these processes may account for the unusual positive slopes of CSD for smaller crystals (Fig. A1). Size distributions of zircons in low- $\delta^{18}\text{O}$ lavas are similar to those in other rocks, as are their average zircon saturation temperatures and corresponding whole-rock concentrations of zirconium (Table 2). However, the zircon CSD trends shown in Fig. A1 do not necessarily indicate a single episode of growth for a single zircon population

from a cooling magma. CSD are a time-integrated picture. We argue below that many zircons are xenocrysts and thus the size distribution is partially inherited from the source rock, and may include stages of zircon dissolution and overgrowth.

Imaging and trace element profiling

Yellowstone zircons, like many igneous zircons worldwide, exhibit euhedral morphologies but complex internal structures caused by trace element zonation (Fig. A2). Examination of external shapes of zircons by secondary electron microscopy reveals that many zircons form aggregates and show features indicative of zircon growth on, or together with, magnetite and apatite. Back-scattered, secondary electron, and CL images of polished zircon grain mounts reveal that most zircons have oscillatory zonation, often with sector zoning (80% of all crystals, Fig. A2a and b). Zircons with resorbed cores, where zoning in the cores is truncated by the zoning in the rims, constitute ~ 5 –20% (Fig. A2c). Fewer than 5% of grains have dark and irregularly shaped cores (Fig. A2d).

Trace element profiles of Hf, U, Th, P, Y and Ce concentrations were made by electron microprobe across the four zircon types described above (Fig. A2). Trace elements show a clear correlation with CL: darker CL zones are richer in Y, Th and U. Different sector zones

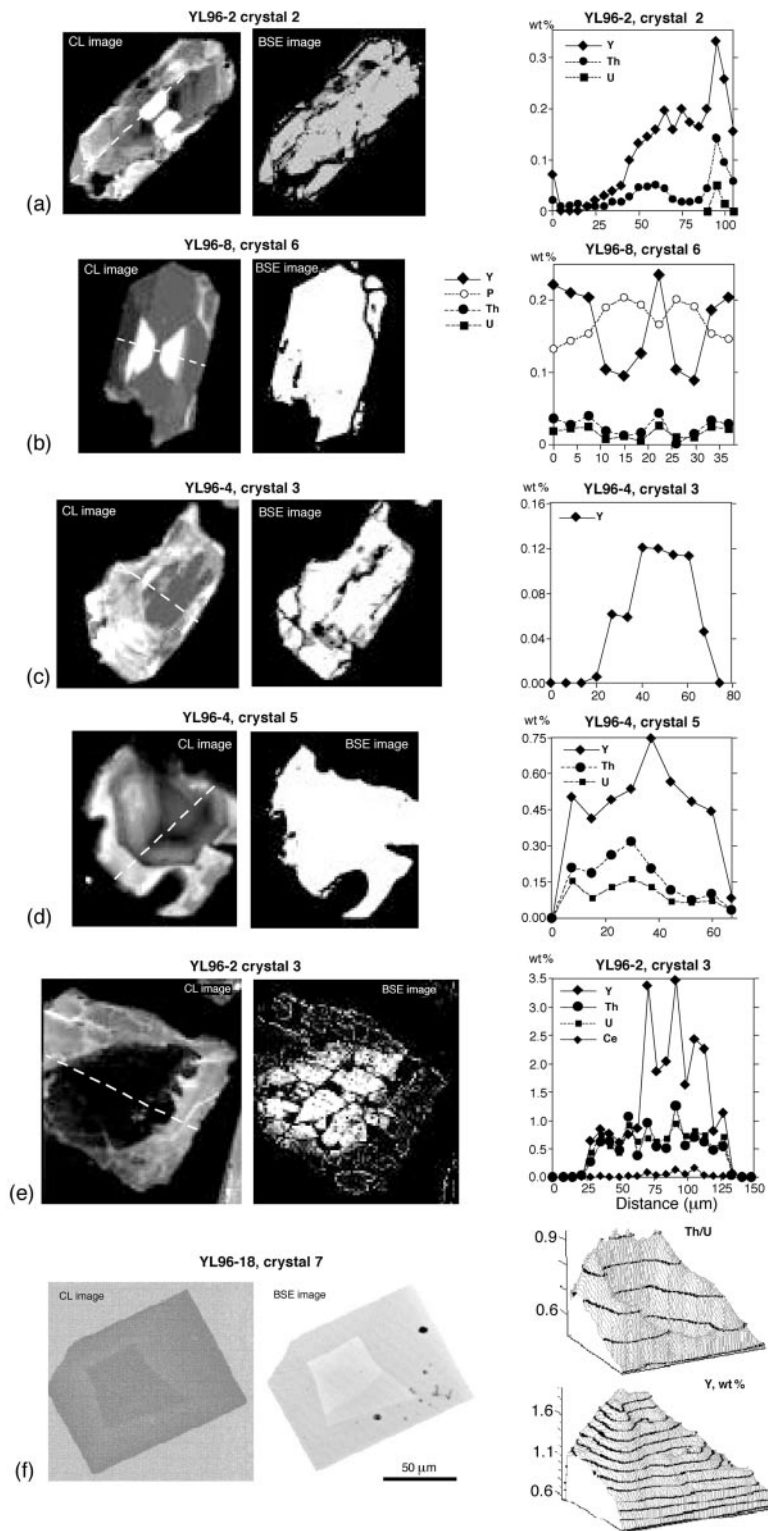


Fig. A2. Cathodoluminescence images and trace element profiles (dashed line) through zircons from Yellowstone rhyolites. (Note up to one order of magnitude variation in Y concentrations between dark and light zones.) Detection limits were: 105 ppm Th, 57 ppm Y and Ce, 70 ppm U, 211 ppm P. Maps (f) show the distribution of Y and Th/U in one selected zircon crystal, based on 109 point analyses (Fournelle *et al.*, 2000).

in a single crystal exhibit a factor of two variation in concentrations of trace elements, especially Y (Fig. A2b). Dividing the measured Y concentrations in zircons by the appropriate zircon–melt partition coefficient (Hinton & Upton, 1991) yields magmatic concentrations. For most zircon grains with $<2\times$ variations within different sectors in one grain, the reconstructed equilibrium magmatic concentrations of Y are within that measured in Yellowstone rhyolites, 40–60 ppm (Table 2).

Quantitative maps of trace element concentrations were made on several grains (Fig. A2f) (Fournelle *et al.*, 2000). The results show complicated patterns of trace element distribution within many zircon crystals from low- $\delta^{18}\text{O}$ lavas, but more regular patterns in LCT and HRT. In particular, wide variations in concentrations (Y and Th vary by 2.5 orders of magnitude in a single

crystal, whereas Th/U ratio varies by a factor of three) cannot be ascribed to a single episode of zircon growth from a magma with equilibrium partitioning, given the published ranges of zircon–melt partition coefficients (Hinton & Upton, 1991). Rather, these zircons are derived from related plutonic (subvolcanic) rocks (e.g. Bacon *et al.*, 2000) and record nearly complete crystallization, or a series of crystallization–dissolution events.

We conclude that trace element abundance and distribution in zircon, unlike isotopic ratio and age information, is of limited importance for making unambiguous petrogenetic inferences on the composition of coexisting melt. Trace elements in zircon are more dependent on local variations in concentration in the source, and kinetics of zircon crystallization–overgrowth (e.g. Hoskin & Ireland, 2000).